This manuscript is a non-peer-reviewed preprint submitted to EarthArXiv. It has been submitted to a peer-reviewed journal for publication.

Where to Watch the Water: Multi-Sensor Network Design Optimization for Inland Flood Detection

Basit A. Akinade[1,2], Amobichukwu C. Amanambu[1,2,*], and M. A. Lisa Davis[2]

[1]*Water INtelligence and Geospatial Sensing (WINGS) Laboratory, Department of Geography and the Environment, The University of Alabama, Tuscaloosa, AL, USA*

[2]*Department of Geography and the Environment, The University of Alabama, Tuscaloosa, AL, USA*

[*]*Corresponding author:* acamanambu@ua.edu

Abstract

Inland flood detection is often constrained less by sensor availability than by where sensors are placed along branching river networks, especially in ungauged headwaters where floods often initiate. We present a three-phase, decision-focused framework for designing basin-by-basin multi-sensor flood detection networks that coordinate water-level, discharge, and camera sensors while explicitly balancing risk-weighted detection, false-alarm penalties, and deployment cost. Using greedy submodular optimization across 65 HUC10 basins in the Southern Appalachians, we generated four operational scenarios spanning coverage-maximizing to resource-constrained deployments, with 491 to 216 potential sensor locations, respectively, with observed diminishing returns. Across scenarios, optimized networks consistently outperform common allocation baselines (random and uniform-grid placement), with improvements over random placement rising from 36.8% under the maximum-coverage design to 77.3% under the resource-constrained design, and remaining about 59.5% under the intermediate configurations. We then validate hydrologic relevance using 44 years (1979–2023) of National Water Model Retrospective v3.0 streamflow, showing that selected sites are systematically located on higher-flow river segments relative to a spatially independent reference set. Finally, we quantify complementarity with 69 existing USGS gages, demonstrating that optimized networks act as modular add-ons that expand risk-weighted coverage from 44.3% (USGS-only) to as high as 96.7% when combined, while supporting a cascade warning architecture with median upstream lead times of ∼2 hours. The results provide a scalable framework for expanding flood monitoring to maximize early-warning value per sensor deployed.

Plain Language Summary

Flood warnings are more difficult in places where few streamgages monitor the small upstream streams where high flows often begin. This paper presents a method for deciding where to place a limited number of low-cost multisensor stations that combine water-level sensors, discharge sensors, and cameras at the same location. The method prioritizes locations with higher flood risk, avoids placing stations in lower-risk areas, and can be adjusted for different budgets and tolerance for false alarms. We applied the approach across the Southern Appalachians and tested whether the selected sites correspond with river reaches that experience high flows using 44 years of national-scale streamflow simulations. We also evaluated how these stations would complement the existing U.S. Geological Survey streamgage network and found that upstream stations can provide earlier warning of flood development before high flows reach downstream gages. The result is a reproducible framework for expanding flood monitoring and improving early warning in ungaged headwaters and downstream communities.

1 Introduction

The global hydrometric network is contracting at precisely the moment when flood risk is expanding. An estimated 20 to 30 percent of stream gauging stations worldwide have been decommissioned since the 1980s due to funding constraints and institutional fragmentation, leaving vast portions of river networks unmonitored (Fekete et al., 2015; Krabbenhoft et al., 2022). This observation crisis persists despite technological advances that now enable low-cost, Internet of Things (IoT)-enabled, multi-parameter flood sensing at scales unimaginable a generation ago (Tauro, Petroselli, & Grimaldi, 2018; McCabe et al., 2017; Kabi, wa Maina, Mharakurwa, & Mathenge, 2023). Yet technology alone cannot resolve the fundamental spatial allocation problem: where, among thousands of potential sensor locations, should limited monitoring resources be deployed to achieve maximum flood detection benefit? Traditional network design approaches guided by expert judgment, historical precedent, or proximity to population centers lack the mathematical rigor to navigate complex trade-offs between detection coverage, spatial redundancy, cost constraints, and complementarity with existing infrastructure (Keum & Coulibaly, 2017; Tien, Lozano, & Chavan, 2023; Andrews & Grantham, 2024). Addressing this challenge requires reframing flood monitoring network design as an optimization problem amenable to principled algorithmic solutions.

The monitoring deficit is particularly acute for inland flood detection, where drainage networks exhibit dendritic complexity spanning orders of magnitude in contributing area within single watersheds. Unlike coastal flooding along major corridors, inland floods emerge from tributary convergences, propagate through nested sub-basins, and demand spatially distributed observation to capture event onset before downstream accumulation reaches catastrophic thresholds (Gourley et al., 2017). Smaller tributaries where flood waters often originate are largely unmonitored, with gauge networks dominating in large perennial rivers (Krabbenhoft et al., 2022). Effective early warning thus depends not on densifying observation along already-monitored mainstems, but on strategic extension into ungauged headwaters where flood genesis occurs (Emerton et al., 2016; Nearing et al., 2024). This imperative grows more urgent as climate change intensifies precipitation extremes (Tabari, 2020; Milly, Wetherald, Dunne, & Delworth, 2002; Amanambu et al., 2020) and development extends into flood-prone landscapes (Wing et al., 2018; Tellman et al., 2021). Early warning systems represent proven, cost-effective climate adaptation measures, with investments yielding returns of 3–16 billion dollars annually in avoided losses (World Meteorological Organization, 2022; Hallegatte, 2012). Taken together, these factors make flood sensor network optimization a coverage problem across hierarchical stream networks, constrained by existing infrastructure, deployment costs, detection physics, and the need to maximize public safety benefit per monitoring dollar.

Prior research on hydrometric network optimization has pursued two principal traditions. Information-theoretic methods that maximize entropy or minimize redundancy among potential sensor sites, selecting locations that collectively capture maximum hydrological variability (Alfonso, Lobbrecht, & Price, 2010; Samuel, Coulibaly, & Kollat, 2013; Mishra & Coulibaly, 2009). While mathematically elegant, these approaches optimize for representativeness rather than flood detection specifically, potentially underweighting high-risk headwaters. Alternatively, heuristic and multi-objective frameworks incorporate flood-relevant criteria but often do not provide guarantees on how close the selected network is to the optimal solution and may scale poorly as the number of candidate sites grows (Keum & Coulibaly, 2017; Farahmand, Liu, Dong, Mostafavi, & Gao, 2022). Recent advances in submodular optimization offer a principled middle path with provable approximation bounds (Krause, Leskovec, Guestrin, VanBriesen, & Faloutsos, 2008; Oh & Bartos, 2025), while observability-based approaches have demonstrated success for contaminant tracing applications (Bartos & Kerkez, 2021). Critically, however, existing frameworks share three common limitations. They largely treat network design in isolation from existing monitoring infrastructure, missing opportunities to quantify complementarity with existing gauge networks. They focus predominantly on single-sensor deployments rather than coordinated multi-sensor systems capable of distributed flood detection. Also, they

rarely validate optimized placements against long-term hydrological records that establish whether selected locations actually experience the flood magnitudes of operational concern.

This study addresses these gaps by developing a multi-sensor flood detection network optimization framework. We present what is, to our knowledge, the first framework that jointly optimizes multi-sensor inland flood detection networks and quantifies functional complementarity with existing gage infrastructure through a multi-indicator upstream classification, validated against multi-decadal retrospective discharge records. Therefore, we formulate sensor placement as a greedy submodular maximization problem that incorporates spatially heterogeneous flood risk indices, detection-radius constraints, and value scenarios reflecting operational trade-offs. Our specific objectives are: (1) to develop an optimization algorithm that jointly considers spatial coverage, flood risk weighting, and coordination among multiple sensors (water level, discharge & camera); (2) to validate network performance using the National Water Model Retrospective v3.0 dataset spanning 1979 to 2023 to establish that optimized placements target reaches with significantly higher flood discharge potential than random alternatives; (3) to propose sensor expansion, complementing existing infrastructure through systematic integration analysis.

2 Study Area and Data

2.1 Study Area

The study area encompasses 65 HUC10 watersheds (34,569 km^2) in a Southern Appalachian region, spanning portions of North Carolina, Tennessee, South Carolina, Georgia, and Virginia (Figure 1). The region lies primarily within the Blue Ridge physiographic province, characterized by steep terrain (mean slope >15° in headwaters), dense drainage networks, and elevations ranging from 300 m to over 2,000 m. The existing USGS stream gage network comprises 69 operational stations. The region was selected based on four criteria: (1) flash flood fatality rates exceeding national averages (Ashley & Ashley, 2008), exemplified by Hurricane Helene (September 2024), which caused more than 250 deaths, with catastrophic inland flooding across the southern Appalachians (Britannica, 2024; Hagen, Cangialosi, Chenard, Alaka, & Delgado, 2026); (2) diverse flood-generating mechanisms including convective storms, tropical cyclone remnants, and extratropical systems (Gaffin & Hotz, 2000; Smith, Baeck, Ntelekos, Villarini, & Steiner, 2011); (3) topographic complexity across 1,700 m of relief where terrain-locked convective systems dominate extreme flood production (Sturdevant-Rees, Smith, Morrison, & Baeck, 2001); (4) documented monitoring gaps in headwater catchments where warning times are shortest (Golden, Christensen, McMillan, et al., 2025).

2.2 Data Sources

This study integrates geospatial datasets to characterize potential sensor sites and validate network performance (Table 1). The primary stream network was derived from NHDPlus High Resolution, providing 238,019 Potential Sensor Locations (PSLs) with inherited hydrological attributes across 65 HUC10 watersheds.

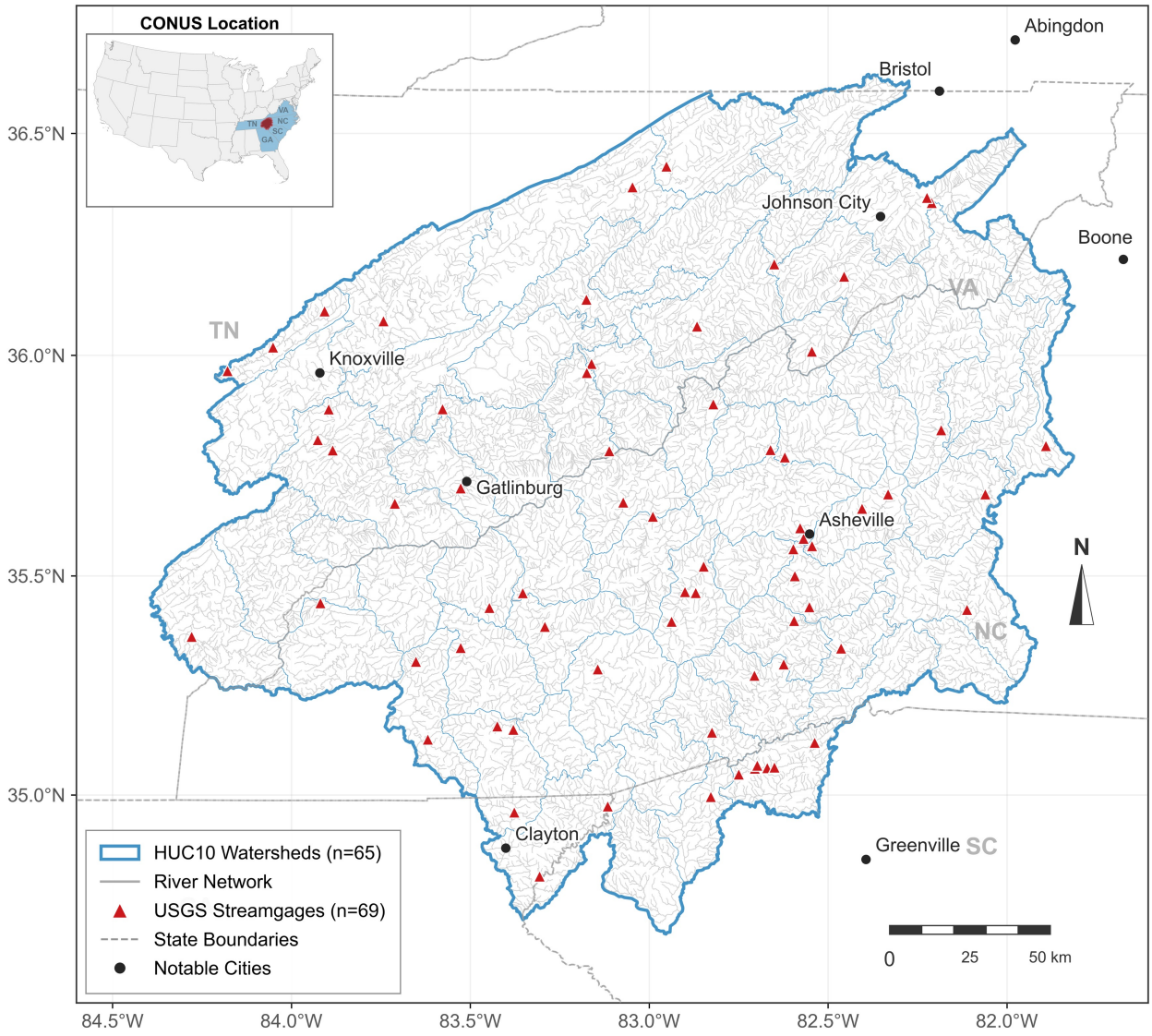

Figure 1: Study area in the Southern Appalachian region showing 65 HUC10 watersheds. HUC10 watershed boundaries were obtained from the U.S. Geological Survey NHDPlus High Resolution dataset (Moore et al., 2025). The map also shows the river network, USGS streamgages, state boundaries, and notable cities.

Table 1: Summary of datasets used in multi-sensor flood detection network optimization.

Data Category	Dataset	Spatial Res.	Temporal Coverage	Source	Key Variables Used
Stream Network & Hydrology	NHDPlus High Resolution (HR)	1:24,000	Static	USGS	Flowlines (network geometry) and PSLs; drainage area, flow accumulation, Strahler stream order, stream level, channel slope, upstream network length, HUC10 boundaries, lake fraction
Terrain & Topography	3D Elevation Program (3DEP) DEM	10 m	Static	USGS	Elevation, terrain slope, and topographic wetness index (TWI)
Precipitation	Multi-Radar Multi-Sensor (MRMS) Quantitative Precipitation Estimates	1 km	Hourly (2020–2024)	NOAA NSSL	Mean annual precipitation (derived from hourly MRMS QPE, 2020–2024)
Flood Risk & Hazard	FEMA National Risk Index (NRI)	Census tract	Static	FEMA	Riverine flood event frequency and riverine expected annual loss (used to construct the tract-based flood-risk surface R).
Monitoring Infrastructure	USGS Streamgages	Point locations	Static	USGS NWIS	Station coordinates, 69 active gages within study domain
Validation	National Water Model (NWM) Retrospective v3.0	NHDPlus reach	Hourly (1979–2023)	NOAA/ OWP	Hourly simulated streamflow used to compute annual mean flow, high flow percentiles (Q_{95}, Q_{99}), mean annual maximum flow, and flashiness index.

3 Methods

3.1 Selection of Potential New Sensor Locations

PSLs were derived using the NHDPlus High Resolution hydrographic network (Moore et al., 2025) by extracting the downstream terminus of each flowline segment across 65 HUC10 watersheds. This approach ensures PSLs occupy points of maximum contributing drainage area where integrated discharge signals are strongest, consistent with established stream gauging principles (Rantz et al., 1982; Sauer & Turnipseed, 2010). Reach endpoints also correspond to natural hydraulic control points; confluences, slope breaks, and channel constrictions, where stage–discharge relationships tend to be more stable (Herschy, 2009). Unlike grid-based or random sampling schemes that do not enforce standard sensor site-selection criteria and can yield operationally unsuitable PSLs (Sauer & Turnipseed, 2010), network-constrained site selection ensures every PSL lies directly on the hydrographic network with inherited routing topology, ensuring upstream–downstream connectivity analysis (Moore et al., 2025). Each PSL retained hydrological attributes from its parent flowline segment (drainage area, Strahler stream order, channel slope, lake fraction, etc.). Terrain derivatives, including local channel slope, hillslope gradient, and topographic wetness index, were extracted from the 3DEP 10-m digital elevation model (U.S. Geological Survey, 2019) at each PSL coordinate following standard practice in catchment characterization (Addor, Newman, Mizukami, & Clark, 2017). Flood risk metrics, including expected annual flood loss frequency and expected annual flood loss, were derived from FEMA National Risk Index census tracts (Federal Emergency Management Agency, 2025).

3.2 Overview of the Optimization and Validation Framework

Given the candidate set of Potential Sensor Locations (PSLs) derived in Section 3.1, the optimization and validation proceed in three phases (Figure 2). Table 1 summarizes the input datasets, their spatial and temporal resolution, sources, and key variables. Phase I employs basin-by-basin greedy submodular optimization to identify optimal sensor placements within each HUC10 watershed (Krause & Golovin, 2014). Phase II evaluates whether the selected sites coincide with reaches that exhibit higher flood discharge magnitudes relative to randomly selected locations, using 44 years (1979 to 2023) of National Water Model Retrospective v3.0 simulated streamflow (Cosgrove et al., 2024), with comparisons based on high-flow percentiles (Q_{99}),

mean annual maximum discharge, and flashiness indices. Phase III quantifies integration synergies with the existing USGS stream gage infrastructure and classifies proposed sensors by their functional role in a flood warning cascade architecture.

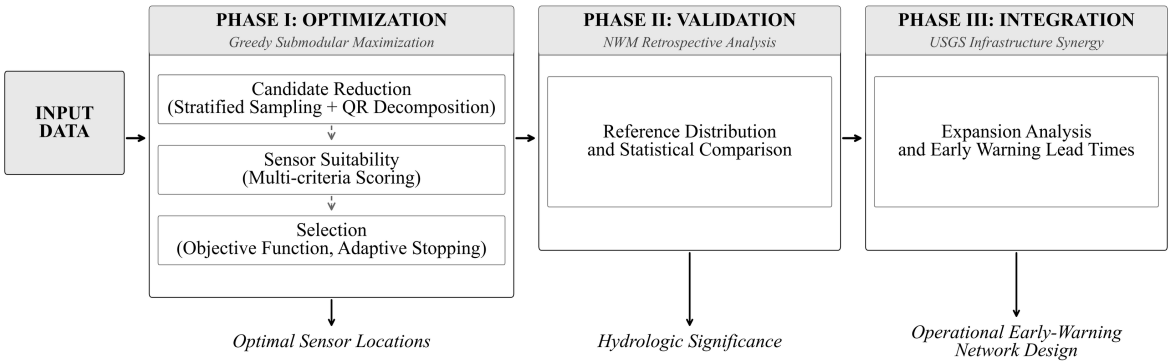

Figure 2: Three-phase methodological framework for multi-sensor flood detection network design, combining greedy submodular optimization (Krause & Golovin, 2014), NWM Retrospective v3.0 validation (Cosgrove et al., 2024), and USGS stream gage infrastructure synergy analysis.

The algorithm processes each HUC10 watershed independently to respect hydrologic boundaries (Seaber, Kapinos, & Knapp, 1987), then merges cross-boundary redundancies to produce a spatially coherent regional network. Four operational scenarios (maximum coverage, balanced risk-cost, infrastructure-complementary, and budget-constrained) spanning different management priorities enable stakeholders to select network configurations aligned with their risk tolerance and resource constraints.

3.3 Reduction of Potential Sensor Locations

The full set of PSLs (with variables in Table 1) within each HUC10 watershed must be reduced to a computationally tractable subset that preserves spatial coverage and hydrological diversity before optimization can proceed. Given N potential sites within a basin, direct optimization becomes computationally prohibitive due to $O(N^2)$ pairwise distance calculations. We employed a two-stage reduction combining stratified spatial sampling (Cochran, 1977) with column-pivoted QR decomposition (Businger & Golub, 1965). The first stage partitions PSLs by geographic grid cell and flood risk quintile to ensure broad spatial and risk-class representation. The second stage factorizes the weighted feature matrix into an orthonormal matrix Q and an upper-triangular matrix R, then selects pivot columns that capture the greatest independent variation across hydrological attributes. The reduced PSL set S^* is obtained as:

$$S^* = \pi_k\Big(\underbrace{\text{QR-pivot}\Big(\underbrace{\bigcup_{c\in C_\delta}\bigcup_{q=1}^{5}\text{top}_m(C_{c,q},\, R)}_{\text{(I) Stratified sampling}},\ \underbrace{X_w}_{\text{(II) Weighted features}}\Big)}_{\text{(III) QR selection}}\Big) \tag{1}$$

(IV) Final k pivots

where the components are defined as follows:

Component (I): Stratified Spatial Sampling. The first stage partitions PSLs into adaptive grid cells and flood risk quintiles, a stratification that ensures the candidate reduction retains sites spanning the full spectrum of flood exposure from low-risk headwaters to chronically flood-prone reaches:

$$C_{c,q} = \{i \in C : \text{cell}(i) = c \ \wedge \ \text{quintile}(R_i) = q\} \tag{2}$$

with adaptive grid cells C_δ at resolution:

$$\delta = \max\left(0.005°,\ \min\left(0.05°,\ \sqrt{\frac{A_{\text{deg}}}{n_c}}\right)\right) \tag{3}$$

where A_{deg} is the basin's bounding box area in square degrees and $n_c = 500$ is the target cell count, providing sub-kilometer grid resolution at the mean HUC10 basin area (~530 km^2) to ensure adequate spatial partitioning for the subsequent QR decomposition. The $\text{top}_m(C_{c,q}, R)$ selects the $m = 2$ highest-risk sites per cell-quintile combination, ensuring spatial coverage across risk strata while preventing geographic clustering (Cochran, 1977).

Component (II): Spatially Weighted Feature Matrix. The stratified subset is then characterized by a spatially weighted feature matrix incorporating spatial isolation:

$$X_w = X \odot w, \quad w_i = \text{clip}\left(1 + \eta \cdot \frac{\bar{d}_i - \mu_d}{\sigma_d},\ 0.85,\ 1.15\right) \tag{4}$$

where $X \in \mathbb{R}^{n \times p}$ is the standardized feature matrix across the hydrologic attributes (Table 1), $\bar{d}_i$ is the mean distance to $k = 10$ nearest neighbors, μ_d and σ_d are the population mean and standard deviation of isolation distances, and $\eta = 0.15$ controls the isolation adjustment factor. The clip function constrains weights to (0.85, 1.15) to prevent extreme values from dominating selection.

Components (III–IV): QR Pivot Selection. Finally, column-pivoted QR decomposition (Golub & Van Loan, 2013) selects the subset that maximizes hydrological diversity across the reduced candidate set:

$$X_w^T P = QR \ \Rightarrow \ S^* = \{P^{-1}(j) : j = 1, \ldots, k\} \tag{5}$$

where P is the column permutation matrix ordering sites by decreasing linear independence, and the first k pivots form the final reduced PSL solution set. The target size is $k = \max(k_{\min}, \lceil |C'|/\gamma \rceil)$ with $k_{\min} = 100$, and refinement factor $\gamma = 1.3$.

3.4 Flood Risk Quantification

For each PSL, we compute a composite flood risk score integrating historical event frequency and expected annual loss following established indicator-based approaches (Papathoma-Köhle, Cristofari, Wenk, & Fuchs, 2019; Maranzoni, D'Oria, & Rizzo, 2023):

$$R_i = \alpha \cdot E_i^{\text{norm}} + (1 - \alpha) \cdot V_i^{\text{norm}} \tag{6}$$

where E_i^{norm} is the min-max normalized flood event frequency and V_i^{norm} is the normalized expected annual flood loss, both extracted from the FEMA National Risk Index Riverine Flooding module (Federal Emergency Management Agency, 2025). Risk values were derived for each PSL by spatially joining PSL coordinates to the census tract polygons containing them. The weight $\alpha = 0.6$ prioritizes chronically flood-prone locations, where repeated events provide more opportunities for sensor validation and early warning system calibration. Risk scores are re-normalized within each basin to account for inter-basin variability in flood exposure. Sites are assigned to risk tiers $b_i \in \{1, 2, 3, 4, 5\}$, where b_i is the risk bin index for site i used

in the objective function (Section 3.8), corresponding to equal-width quintile boundaries (0 to 0.2), (0.2 to 0.4), (0.4 to 0.6), (0.6 to 0.8), (0.8 to 1.0). Equal-width binning on the re-normalized scores ensures each tier spans an identical proportion of the within-basin risk range, enabling stratified performance evaluation that separately assesses network coverage for low, moderate, and high-risk reaches.

3.5 Sensor Type Suitability Scoring

Each candidate location receives a separate suitability score for discharge gauges, water level sensors, and visual cameras based on local geomorphic, topographic, and hydroclimatic attributes. Discharge gauges favor sites with high flow accumulation and large contributing drainage areas. Water level sensors prioritize locations with high topographic wetness index (Beven & Kirkby, 1979) and gentle slopes. Visual cameras perform best at low-gradient sites but are penalized where high lake fraction degrades performance. All input variables are min-max normalized to (0, 1) prior to combination, with flow accumulation and drainage area log-transformed before scaling (Strahler, 1957). Variable justifications and weights are provided in Tables A1 & A2 (Appendix A). The suitability is therefore formulated as:

$$\boldsymbol{\phi}_i = \begin{bmatrix} \phi_i^{(Q)} \\ \phi_i^{(H)} \\ \phi_i^{(C)} \end{bmatrix} = (\mathbf{W}\,\mathbf{x}_i) \odot \begin{bmatrix} 1 \\ 1 \\ (1 - \gamma\tilde{\psi}_i) \end{bmatrix} \tag{7}$$

where $\phi_i^{(Q)}$, $\phi_i^{(H)}$, and $\phi_i^{(C)}$ denote the discharge-, water level-, and camera-suitability scores at location i. To account for degraded performance of camera-based monitoring over open water (e.g., low texture, glare/reflections, weak bank features), we apply a multiplicative lacustrine penalty only to the camera suitability component. ψ_i denotes the local lake fraction at candidate site i, computed as the proportion of surface-water area classified as lakes/ponds within the camera evaluation footprint; $\tilde{\psi}_i \in [0, 1]$ is the min–max normalized lake fraction across all candidates. The camera score is scaled as $\phi_i^{(C)} \leftarrow \phi_i^{(C)}(1 - \gamma\tilde{\psi}_i)$, where $\gamma \in (0, 1)$ controls penalty strength (here $\gamma = 0.30$). Discharge and stage scores are unchanged (multipliers of 1). A site is classified as deployable for a given sensor type when its suitability score meets or exceeds 0.5, the midpoint of the normalized [0, 1] range, serving as a minimum operational viability criterion.

$$\mathbf{x}_i = \begin{bmatrix} \tilde{A}_{\log,i} \\ \tilde{D}_{\log,i} \\ \tilde{\omega}_i \\ (1 - \tilde{L}_i) \\ \tilde{S}_{c,i} \\ \tilde{P}_i \\ \tilde{I}_i \\ (1 - \tilde{\beta}_i) \\ (1 - \tilde{Z}_i) \end{bmatrix}, \quad \mathbf{W} = \begin{bmatrix} 0.25 & 0.20 & 0.15 & 0.15 & 0.10 & 0.15 & 0 & 0 & 0 \\ 0.15 & 0 & 0.15 & 0 & 0 & 0.15 & 0.20 & 0.20 & 0.15 \\ 0 & 0.15 & 0.15 & 0 & 0 & 0 & 0.20 & 0.25 & 0.25 \end{bmatrix} \tag{8}$$

Predictors are defined as follows: $\tilde{A}_{\log,i}$ log-transformed flow accumulation; $\tilde{D}_{\log,i}$ log-transformed drainage area (km^2); $\tilde{\omega}_i$ Strahler stream order; $\tilde{L}_i$ stream level (so $1 - \tilde{L}_i$ favors mainstems); $\tilde{S}_{c,i}$ channel slope; $\tilde{P}_i$ mean annual precipitation; $\tilde{I}_i$ topographic wetness index (TWI); $\tilde{\beta}_i$ terrain slope (degrees); $\tilde{Z}_i$ elevation (m); $\tilde{\psi}_i$ lake fraction (1 km buffer); γ maximum lake penalty (e.g., 0.30).

3.6 Spatially Adaptive Detection Radius Calibration

The effective detection radius, ρ, for each basin is calibrated from the empirical semi-variogram of flood risk, following geostatistical principles (Matheron, 1963; Cressie, 1993). The experimental semi-variogram is computed as:

$$\hat{\gamma}(h) = \frac{1}{2|N(h)|} \sum_{(i,j)\in N(h)} [R_i - R_j]^2 \tag{9}$$

where $N(h)$ is the set of site pairs separated by lag distance $h \pm \Delta h$. The correlation range a is estimated as the distance at which $\hat{\gamma}(h)$ reaches 95% of the sill (asymptotic semi-variance C):

$$a = \inf\{h : \hat{\gamma}(h) \geq 0.95\, C\} \tag{10}$$

This range represents the spatial scale over which flood risk exhibits autocorrelation, providing a physically meaningful basis for detection radii. Sensor specific detection radii are calibrated as:

$$\rho^{(H)} = 0.9\, a, \quad \rho^{(Q)} = 1.0\, a, \quad \rho^{(C)} = 0.5\, a \tag{11}$$

reflecting the greater spatial representativeness of discharge measurements versus the localized coverage of visual cameras (Merz & Blöschl, 2005). The range a is constrained to $(5, 30)$ km based on typical flood correlation lengths in mesoscale watersheds.

3.7 Detection Probability Model

The probability that sensor j of type t detects a flood event at site i follows an exponential spatial decay model (Zou & Chakrabarty, 2004):

$$p_{ij}^{(t)} = q^{(t)} \cdot \phi_j^{(t)} \cdot \exp\left(-\frac{d_{ij}}{\rho^{(t)}}\right) \cdot \mathbb{1}_{[d_{ij} \leq 2.5\rho^{(t)}]} \tag{12}$$

where $q^{(t)}$ is the baseline detection quality (water level: 0.85, discharge: 0.80, camera: 0.70), reflecting inherent sensor reliability under ideal conditions, d_{ij} is the great circle distance computed through the Haversine formula, and detection is truncated beyond 2.5ρ to enforce finite support.

For a network of selected sensors S, the combined detection probability at site i uses the probabilistic union assuming conditional independence across sensor types:

$$P_i(S) = 1 - \prod_{t\in\{H,Q,C\}} \left(1 - \max_{j\in S} p_{ij}^{(t)}\right) \tag{13}$$

A multi-sensor synergy adjustment, $\Delta = 0.15$, is applied when at least two sensor types exceed a detection threshold $\tau_{\text{syn}} = 0.10$ at high-risk sites ($R_i \geq 0.30$), reflecting the enhanced reliability of corroborated detections (Krzhizhanovskaya et al., 2011):

$$P_i^*(S) = \min\left(1,\ P_i(S) + \Delta \cdot \mathbb{1}_{[M_i \geq 2]} \cdot \mathbb{1}_{[R_i \geq 0.30]} \cdot R_i\right) \tag{14}$$

where M_i counts sensor types with detection probability exceeding τ_{syn} at site i.

3.8 Objective Function and Greedy Maximization

Performance Metrics. The risk-weighted true positive rate (detection coverage) quantifies the fraction of total flood risk monitored by the network:

$$\mathrm{TP}(S) = \frac{\sum_{i=1}^{N} R_i \cdot P_i^*(S)}{\sum_{i=1}^{N} R_i} \tag{15}$$

For low-risk sites ($R_i < \tau_{\text{low}} = 0.20$), false positive rate captures unnecessary monitoring of flood unlikely locations:

$$\mathrm{FP}(S) = \frac{\sum_{i:\, R_i < \tau_{\text{low}}} (1 - R_i) \cdot P_i^*(S) \cdot R_i}{\sum_{i:\, R_i < \tau_{\text{low}}} (1 - R_i)} \tag{16}$$

The raw network performance objective balances detection and false alarms:

$$J(S) = \mathrm{TP}(S) - \lambda \cdot \mathrm{FP}(S) \tag{17}$$

where λ is the false positive penalty weight controlling the detection precision trade-off.

Marginal Value Threshold Adjusted Objective. To prevent network over-expansion and identify the point of diminishing returns, we introduce a per-sensor deployment marginal value threshold (Krause, Singh, & Guestrin, 2008):

$$J_c(S) = J(S) - c \cdot |S| \tag{18}$$

The cost parameter $c = \tau \cdot \Delta J_1$ is calibrated as a fraction τ of the first sensor's marginal gain ΔJ_1, ensuring the threshold scale adapts to basin specific flood dynamics.

Greedy Selection with Spacing Constraints. Sensors were selected iteratively through greedy submodular maximization, which guarantees a $(1 - 1/e)$ approximation ratio for monotone submodular functions (Nemhauser, Wolsey, & Fisher, 1978):

$$s^* = \arg\max_{s \notin S} \left[J_c(S \cup \{s\}) - J_c(S) \right] \quad \text{s.t.} \quad d(s, S) \geq d_{\min}(s) \tag{19}$$

The minimum spacing constraint prevents sensor clustering:

$$d_{\min}(s) = 0.4\, \rho^{(Q)} \cdot f(b_s), \quad f(b) = \begin{cases} 0.6 & b \geq 4 \\ 1.0 & \text{otherwise} \end{cases} \tag{20}$$

where b_s is the risk tier, allowing denser placement in high-risk areas. Selection terminates when marginal gains become non-positive over a plateau window of $w = 5$ consecutive iterations, with a conservative implementation cap of $K_{\max} = 100$ sensors per basin to bound runtime. Also, due to floating-point precision differences across computing platforms, sensor counts may vary by ±3–5% when executed on different hardware.

3.9 Operational Scenario Framework

We define four operational scenarios spanning a 2×2 factorial design over the false positive penalty (λ) and marginal value threshold (τ), enabling stakeholders to select network configurations aligned with management and budget priorities (Table 2):

Each scenario produces a distinct network configuration. We selected scenario B to serve as the primary baseline for comparisons, while scenarios A, C, and D provide sensitivity bounds for operational planning.

Table 2: Operational scenarios for network configuration.

Scenario	λ	τ	Operational Interpretation
A: Maximum Coverage	0.10	0.02	Prioritize detection; tolerate false alarms; flexible budget
B: Balanced	0.15	0.05	Trade-off between coverage and precision (baseline)
C: Precision-Focused	0.25	0.05	Minimize false alarms; maintain moderate network size
D: Resource-Constrained	0.15	0.10	Limited deployment capacity; highest-value sensors only

3.10 Cross-Basin Edge Merging

Adjacent HUC10 basins may independently place sensors near shared boundaries, creating spatial redundancy. We identified cross-boundary sensor pairs (i, j) with $d_{ij} < d_{\text{merge}} = 5$ km and retain only the higher suitability sensor:

$$\text{Remove } i \text{ if } \bar{\phi}_i < \bar{\phi}_j \text{ and } \text{HUC10}(i) \neq \text{HUC10}(j) \tag{21}$$

where $\bar{\phi} = \frac{1}{3}(\phi^{(H)} + \phi^{(Q)} + \phi^{(C)})$ is the mean suitability across sensor types.

3.11 Baseline Comparisons

Algorithm performance is benchmarked against alternative selection strategies evaluated at equivalent network size K:

1. *Random*: Uniform random selection respecting spacing constraints ($n = 10$ trials)
2. *Uniform Grid*: Nearest sites to regular $\sqrt{K} \times \sqrt{K}$ grid centroids

Each baseline is evaluated using the J-score objective (Eq. 17) with all four operational scenarios. The multi-sensor algorithm's improvement over baselines is quantified as the percentage difference between the multi-sensor J-score and the baseline J-scores.

3.12 Sensitivity and Robustness Analysis

We assessed the algorithm robustness through three complementary analyses: *detection radius uncertainty* evaluated by applying multipliers $m \in \{0.70, 0.85, 1.00, 1.15, 1.30\}$ to the calibrated detection radii and recomputing network performance without re-optimization, where stable performance across multipliers indicates limited sensitivity to radius specification; *sub-modularity verification* follows the greedy-optimization requirements of Nemhauser et al. (1978) by checking for diminishing marginal returns along the selection sequence, operationalized as monotonically decreasing marginal gains for at least 70% of basins; and the *Pareto frontier* is characterized by evaluating optimized networks at $K \in \{5, 10, 15, 20, 30, 50, 75, 100\}$ sensors and computing the resulting TP–FP trade-off, which quantifies the rate of diminishing returns with increasing network density and supports identification of efficient operating points where improvements in detection require either higher false positives or additional deployments.

3.13 Model Validation

To verify that optimized sensor locations correspond to hydrologically significant stream reaches rather than artifacts of the optimization process, we validate selected sites against the NOAA National Water Model (NWM) Retrospective Analysis v3.0 (Cosgrove et al., 2024).

3.13.1 Flow Regime Metrics

For each matched NWM reach, we computed five flow regime metrics characterizing hydrologic significance. Annual mean flow (AMA) was calculated as the arithmetic mean of hourly streamflow across the full record length (approximately 386,000 hours). High-flow percentiles (Q_{95} and Q_{99}) were derived from the empirical cumulative distribution function of hourly flows, representing thresholds exceeding 5% and 1% of the time, respectively (Smakhtin, 2001). The annual maximum flow (AMAX) was computed as the mean of annual peak flows across complete water years, following standard practice in flood frequency analysis (Stedinger, Vogel, & Foufoula-Georgiou, 1993). Finally, the flashiness index was calculated as the ratio Q_{99}/Q_{95}, where values substantially exceeding 1.0 indicate flashy hydrologic response characteristic of flood-prone streams (Baker, Richards, Loftus, & Kramer, 2004).

3.13.2 Reference Distribution Construction

To establish a null expectation for statistical comparison, we constructed a reference distribution from 10,000 randomly sampled PSLs that explicitly exclude all selected sensor locations from all scenarios. The exclusion criterion was applied across all four operational scenarios simultaneously:

$$C_{\text{ref}} = C_{\text{all}} \setminus \bigcup_{k \in \{A,B,C,D\}} S_k \tag{22}$$

where C_{all} represents the complete set of PSLs and S_k denotes the selected sensor set for scenario k. Reference points were sampled uniformly at random with a fixed seed for reproducibility. Of the 10,000 sampled reference PSLs, 9,647 had valid NWM metrics and were retained for the validation analysis.

3.13.3 Hydrologic Significance Testing

We tested the hypothesis that selected sensor sites correspond to systematically larger, more flood-prone stream reaches than random PSLs using nonparametric methods robust to non-normal distributions. The Mann-Whitney U test evaluated whether selected sites exhibited stochastically larger flow metrics than reference sites, with the null hypothesis that a randomly chosen selected site has equal probability of exceeding or being exceeded by a randomly chosen reference site (Mann & Whitney, 1947). Effect size was quantified using Cliff's delta, which measures the probability that a randomly selected sensor site has a larger flow metric than a randomly selected reference site, minus the reverse probability (Cliff, 1993). Effect size interpretation followed Romano, Kromrey, Coraggio, and Skowronek (2006): $|\delta| < 0.147$ negligible, $0.147 \leq |\delta| < 0.33$ small, $0.33 \leq |\delta| < 0.474$ medium, and $|\delta| \geq 0.474$ large. The Kolmogorov-Smirnov test assessed whether entire distributions differed, with sensitivity to differences in shape, location, and scale (Massey, 1951).

3.13.4 Percentile Exceedance Analysis

We computed the percentage of selected sensors exceeding reference distribution percentiles to quantify systematic selection bias toward high-flow reaches. Under the null hypothesis of random selection, approximately 50% of sensors would exceed the reference median, 25% would exceed the 75th percentile, and 10% would exceed the 90th percentile. Systematic exceedance of these thresholds would indicate that the algorithm preferentially selects hydrologically significant reaches.

3.13.5 Absolute Threshold Analysis

We evaluated the fraction of sensors on streams exceeding operationally meaningful discharge thresholds:

$$f_{\geq\theta}(S) = \frac{|\{s \in S : Q_{99,s} \geq \theta\}|}{|S|} \tag{23}$$

where $\theta \in \{1, 5, 10, 50\}$ m^3s^{-1}. These thresholds correspond approximately to small creeks (1 m^3s^{-1}), moderate streams (5 m^3s^{-1}), significant rivers (10 m^3s^{-1}), and major rivers (50 m^3s^{-1}), providing operational context for network deployment planning (Wohl, 2017).

3.14 Existing Stream Gage Network Integration Analysis

3.14.1 Coverage Quantification

We quantified weighted flood risk coverage for any station set X as the fraction of total risk within detection range (Pappenberger et al., 2015). Let U denote the set of n_U existing USGS stream gages and S the proposed sensor network:

$$\Gamma(X) = \frac{\sum_{i:\, d(i,X)\leq\rho} R_i}{\sum_{i=1}^{N} R_i} \tag{24}$$

where $d(i, X) = \min_{j\in X} d_{ij}$ is the distance from PSL i to the nearest station in set X, ρ is the detection radius, and R_i is the flood risk weight at site i. Network synergy, the incremental coverage gained by augmenting USGS infrastructure with proposed sensors, is quantified as:

$$\Delta\Gamma = \Gamma(U \cup S) - \Gamma(U) \tag{25}$$

and redundancy ratio:

$$\eta_{\text{red}} = \frac{\Gamma(U) + \Gamma(S) - \Gamma(U \cup S)}{\Gamma(S)} \tag{26}$$

3.14.2 Multi-Indicator Upstream Classification

Upstream relationships between proposed sensors and USGS stations were determined using a multi-indicator framework combining four NHDPlus HR-derived hydrological attributes. For sensor s and USGS station u within the same HUC10 watershed, the composite upstream score is:

$$\Phi(s, u) = \mathbb{1}[Z_s - Z_u > \delta_z] + \mathbb{1}[\omega_s \leq \omega_u] + \mathbb{1}[A_s < A_u] + \mathbb{1}[L_s < L_u] \tag{27}$$

where Z is elevation (m), ω is Strahler stream order, A is flow accumulation (contributing cells), L is upstream network length (km), $\delta_z = 10$ m is the minimum elevation threshold, and $\mathbb{1}[\cdot]$ is the indicator function returning 1 if the condition is true and 0 otherwise. These indicators reflect fundamental drainage network properties: upstream positions exhibit higher elevation, lower or equal stream order, smaller contributing area, and less accumulated upstream channel length (Strahler, 1957; Tarboton, Bras, & Rodriguez-Iturbe, 1991). Sensor s is classified as upstream of station u if $\Phi(s, u) \geq 2$. Confidence is assigned as high ($\Phi \geq 3$), medium ($\Phi = 2$), or low ($\Phi < 2$), with all classifications requiring the elevation indicator to be satisfied.

3.14.3 Sensor Classification and Functional Roles

We classified the proposed sensors based on proximity to and hydrologic relationship with USGS infrastructure, establishing their functional role in a flood warning cascade (Werner & Cranston, 2009):

(a) **Sentinel:** $d(s, U) > \rho$ and upstream of nearest USGS; Independent early warning in ungauged headwaters. Sensors providing independent coverage in regions beyond USGS detection footprints.

(b) **Cascade Sentinel:** $d(s, U) \leq \rho$ and upstream of nearest USGS; Supplements existing coverage with additional lead time. Sensors located upstream of USGS stations, enabling flood wave detection before arrival at the existing gages.

(c) **Gap Filler:** $d(s, U) > \rho$ and not upstream; Covers monitoring desert in lateral tributaries. Sensors positioned within USGS coverage gaps on tributaries or between stations.

(d) **Validator:** $d(s, U) \leq \rho$ and not upstream; Provides redundancy and cross validation. Sensors co-located with USGS stations for measurement cross-validation.

where ρ is the detection radius and upstream status is determined by the multi-indicator classification ($\Phi \geq 2$) within the same HUC10.

3.14.4 Early Warning Lead Time Estimation

For Cascade Sentinels, we estimate flood wave travel time to the nearest downstream USGS station using kinematic wave theory (Lighthill & Whitham, 1955):

$$T_{\text{lead}} = \frac{d_{\text{Euclidean}} \cdot \kappa}{c} \tag{28}$$

where $d_{\text{Euclidean}}$ is the straight-line distance between sensor and USGS station, $\kappa = 1.3$ is the sinuosity factor accounting for channel meandering, and c is the flood wave celerity:

$$c = v(\omega) \cdot \xi \tag{29}$$

Here $v(\omega)$ is the mean stream velocity indexed by Strahler order and $\xi = 1.5$ is the flood wave celerity factor relative to mean velocity, consistent with kinematic wave theory for natural channels. This formulation yields lead times representing the expected interval between flood detection at an upstream sensor and arrival at the corresponding USGS station.

4 Results

4.1 Study Domain and Potential New Sensor Location Network

The optimization framework was applied to the study area with an initial network comprising 238,019 PSLs, each generated as the downstream terminus of a flowline segment in the NHDPlus High Resolution network. Following stratified sampling and QR decomposition refinement (Section 3), the PSL set was reduced by 96.5% to 8,224 locations while preserving spatial representativeness across flood risk quintiles.

4.2 Operational Scenario Performance

The greedy submodular optimization was executed under four operational scenarios representing distinct management priorities (Table 2). These scenarios span the parameter space defined by false positive penalty weight (λ) and per-sensor cost fraction (τ) yielding network configurations ranging from 216 to 491 sensor locations across the 65 HUC10 study basins. Scenarios B and C converge to nearly identical designs despite different λ values, with overlapping spatial patterns, risk-tier allocations, and detection trajectories (Figure 3; Table 3). Practically, once λ is large enough to suppress high false-positive candidates, further

increments provide limited leverage: the optimization has already excluded low-risk sites that contribute disproportionately to the false positive rate, so additional penalization largely reaffirms the same solution set. All scenarios satisfy the submodularity verification diagnostic with 74–89% of sequential sensor additions exhibiting decreasing marginal gains (Table 3), supporting the applicability of the greedy approximation guarantees across the operational parameter space.

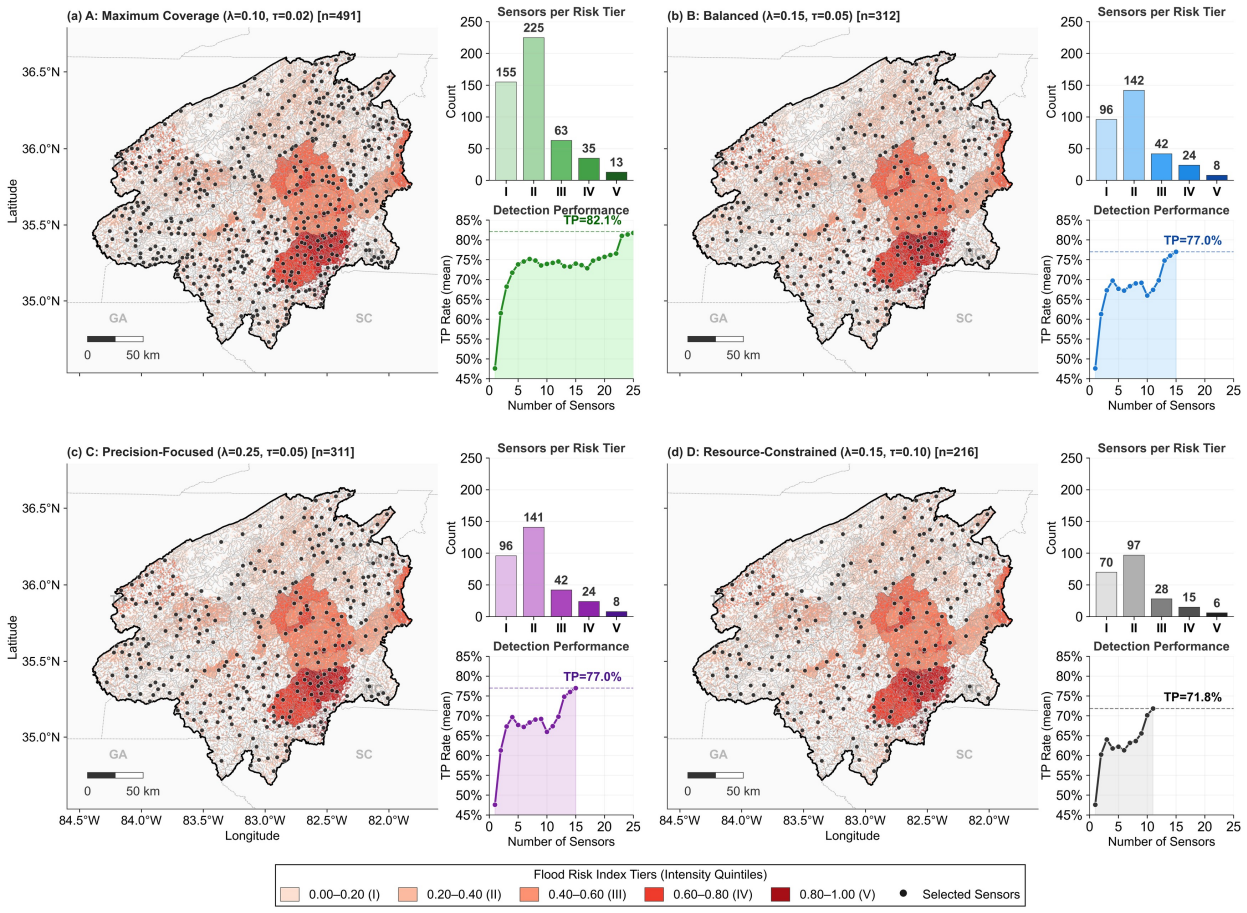

Figure 3: Multi-sensor flood detection network optimization across four operational scenarios. Each panel shows selected sensor locations (black dots) overlaid on flood risk intensity background (quintile classification), sensor distribution by risk tier (upper right histogram), and cumulative detection performance curve showing TP rate convergence with increasing network size (lower right).

Table 3: Network configuration under alternative operational scenarios. TP = true positive rate (flood detection coverage); FP = false positive rate; J = objective function value. Values represent network-wide means; per-basin variability reported as ± standard deviation.

Scenario	λ	τ	Sensors	TP (%)	FP (%)	J-Score	Sensors /Basin	% Decreasing
A	0.1	0.02	491	79.4 ± 11.1	1.8 ± 2.3	0.793 ± 0.111	7.6 (1–26)	89
B	0.15	0.05	312	74.8 ± 10.9	1.5 ± 2.1	0.746 ± 0.109	4.8 (1–15)	81.8
C	0.25	0.05	311	74.7 ± 10.9	1.5 ± 2.1	0.744 ± 0.110	4.8 (1–15)	81.7
D	0.15	0.1	216	69.6 ± 10.7	1.4 ± 2.0	0.694 ± 0.107	3.3 (1–11)	73.7

4.3 Multi-Sensor Advantage over Baseline Methods

Across all operational scenarios, the multi-sensor optimization consistently outperforms both random placement and uniform grid allocation strategies (Table 4), demonstrating that explicitly coordinating heterogeneous instruments yields materially higher flood-detection value than spatially uninformed or geometrically regular placement baselines.

Table 4: Multi-sensor network performance compared to baseline allocation methods across all operational scenarios. Improvement calculated relative to random placement.

Scenario	Method	TP (%)	FP (%)	J-Score	Δ vs. Random (%)
A	Random	58.30	1.30	0.58	—
	Uniform Grid	55.30	1.10	0.55	−5.2
	Multi-Sensor	79.70	1.60	0.80	36.8
B	Random	46.60	1.00	0.46	—
	Uniform Grid	44.60	1.00	0.44	−4.3
	Multi-Sensor	74.20	1.30	0.74	59.5
C	Random	46.60	1.00	0.46	—
	Uniform Grid	44.60	1.00	0.44	−4.3
	Multi-Sensor	74.20	1.30	0.74	59.5
D	Random	39.30	0.80	0.39	—
	Uniform Grid	37.40	0.80	0.37	−4.8
	Multi-Sensor	69.70	1.30	0.70	77.3

The relative advantage is most pronounced under tighter resource constraints (Table 4). As τ increases and the feasible network size contracts, the optimization increasingly prioritizes locations where co-located sensors provide the largest marginal improvement in detection reliability, rather than spreading limited assets thinly across the domain.

Uniform-grid allocation underperformed the random baseline in every scenario, with J-scores of 0.55, 0.44, 0.44, and 0.37 (about 4 to 5% lower than random; Table 4). By contrast, the optimized network clusters along the dominant risk corridors (Figure 4a). Scenario overlap further indicates that the optimization repeatedly returns to a stable subset of high-value sites across alternative operational priorities (Figure 4a).

The suitability profiles of selected sites varied systematically by scenario and sensor type (Figure 4b). Camera-based sensors exhibited the highest mean suitability (0.707 to 0.774) across all scenarios, reflecting the broad availability of low-gradient, low-elevation sites in the study region. Discharge sensors showed more variable suitability (0.521 to 0.590), constrained by channel geometry requirements for accurate flow measurement. These differences arise directly from the scenario parameters defined in Table 2. Under maximum coverage (Scenario A, $\lambda = 0.10$, $\tau = 0.02$), the low cost penalty permits a larger network ($n = 491$) that includes sites across a broader suitability range. As the false positive penalty increases (Scenarios B and C, $\lambda = 0.15$ and 0.25), the optimization progressively excludes low-risk sites, concentrating selections on higher-suitability reaches. Scenarios B and C converge to nearly identical suitability profiles because, beyond a threshold penalty, the pool of high-value candidate sites is effectively fixed and further penalization does not alter site selection. The Resource-Constrained scenario (D, $\tau = 0.10$) achieved the highest mean suitability across all sensor types (Water Level: 0.728; Discharge: 0.590; Camera: 0.774), confirming that tighter resource constraints force the algorithm toward an elite subset of optimally suited locations (Figure 4b).

Across all operational scenarios, the majority of selected sites (86 to 94%) supported co-located multi-sensor deployment (Table 5), with water level and camera sensors exhibiting high suitability at over 89% of locations, while discharge sensor suitability was more selective (52 to 70%). This reinforces that the

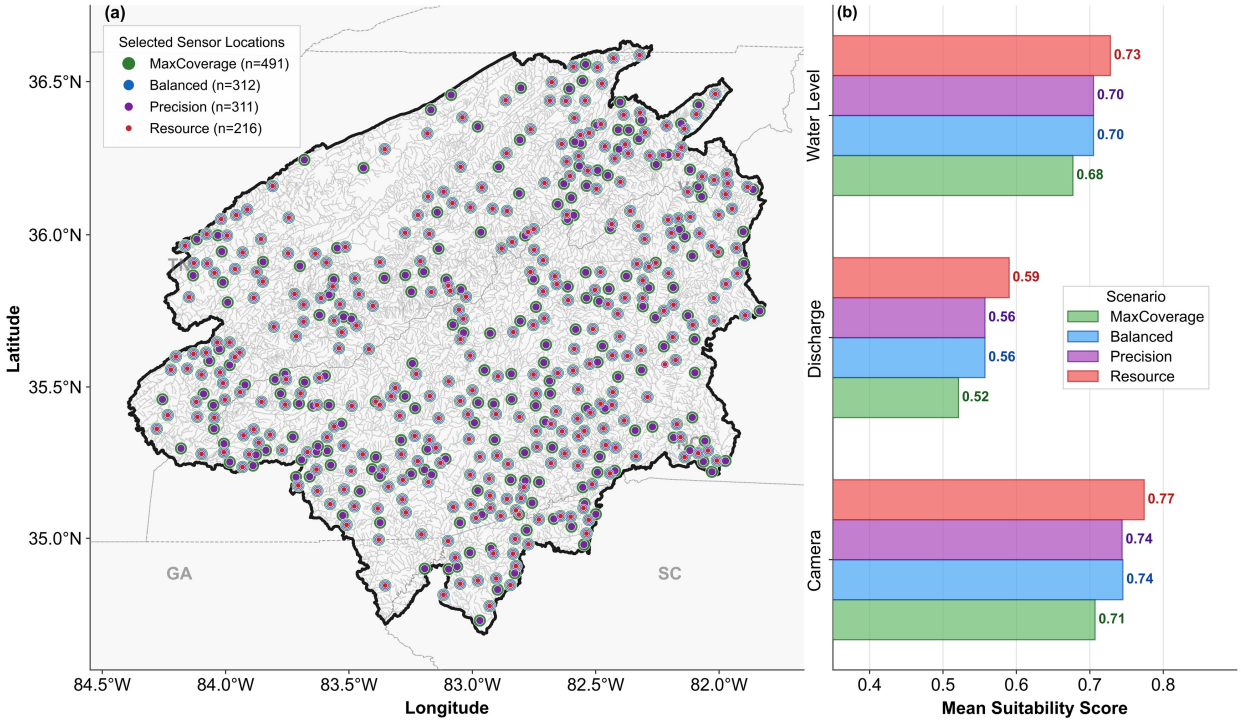

Figure 4: Optimized sensor network configurations across four operational scenarios. (a) Selected sensor locations shown as concentric markers where overlap indicates shared site selection across scenarios (outer: Maximum Coverage; inner: Resource-Constrained). (b) Mean suitability scores by sensor type demonstrate the coverage-quality tradeoff.

Table 5: Sensor type distribution by scenario. Counts indicate sites with suitability score ≥ 0.5 (defined in Section 3) for each type. Suitability weights are defined in Tables A1 and A2 (Appendix A). Co-located sites exceed this threshold for at least two sensor types.

Scenario	Total Sites	Discharge	Water Level	Camera	Co-located Sites
A: Maximum Coverage	491	257 (52%)	444 (90%)	436 (89%)	424 (86%)
B: Balanced	312	193 (62%)	295 (95%)	291 (93%)	284 (91%)
C: Precision-Focused	311	191 (61%)	294 (95%)	290 (93%)	283 (91%)
D: Resource-Constrained	216	152 (70%)	206 (95%)	204 (94%)	202 (94%)

framework's principal performance driver is coordinated multi-sensor placement at a limited number of strategically valuable and operationally feasible sites, rather than broad, single-sensor coverage (Table 5).

4.4 Spatial Distribution and Risk Stratification

Across scenarios, selected sites align with the dominant flood-risk corridors, with the densest deployments consistently anchored in the southeastern high-risk concentration (Figure 3). Risk stratification is also evident in the tier histograms: selections span all five risk quintiles, with the largest counts in the 0.20–0.40 tier (225 of 491 sensors in Scenario A; 97 of 216 in Scenario D), while roughly one quarter are still allocated to tiers ≥0.40 (111 of 491 in A; 49 of 216 in D; Figure 3). This pattern largely follows candidate availability, and the resulting placement remains risk-directed rather than area-directed.

4.5 Detection Radius Calibration and Sensitivity

Basin-specific detection radii, calibrated from semi-variogram analysis (Section 3), ranged from 5.0 to 16.3 km with a mean of 7.6 km. The distribution exhibits strong positive skewness, with approximately half of basins clustering at the minimum threshold, reflecting the steep terrain and rapid hydrologic response characteristic of Appalachian headwaters. Larger detection radii occurred in lower-gradient valley basins where flood signals propagate over greater distances. Sensitivity tests demonstrate that the main conclusions are not contingent on the exact calibration. Across scenarios, objective values increase smoothly with larger radii, and scenario ordering is preserved over the tested range, indicating stability to plausible specification error. The separation between scenarios compresses as radii shrink, consistent with the intuition that smaller footprints reduce the marginal reach of each multisensor location and therefore attenuate the advantage of denser versus sparser networks (Figure 5b).

In operation, the four scenarios occupy distinct points along an efficient detection–precision tradeoff, spanning higher-coverage versus lower-false-positive configurations without dominated solutions. The true positive–false positive tradeoff reveals that all scenarios achieve positions along the Pareto frontier, representing efficient detection-precision balance. Maximum Coverage prioritizes spatial coverage (TP = 79.4%, FP = 1.8%) while Resource-Constrained minimizes false positives (TP = 69.6%, FP = 1.4%), with intermediate scenarios spanning this operational range (Figure 5a).

4.6 Coverage-Marginal Value Tradeoffs (Cost Efficiency) and Submodularity

Across basins, the multi-sensor placement problem shows the diminishing-returns structure that motivates a submodular greedy strategy: the first few selected sites deliver the largest reductions in risk-weighted detection gaps, after which additional deployments yield progressively smaller incremental gains (Figure 6a–b). This pattern is consistent across the four operational scenarios.

Early-ranked selections contribute disproportionately to the achieved objective, and the normalized accumulation curves remain strongly concave relative to a linear reference (Figure 6c–d). Empirical submodularity verification further shows that sequential gains are predominantly decreasing across scenarios (Table 3), supporting the use of greedy selection for this multi-sensor detection objective.

4.7 Model Validation

To assess whether the optimization preferentially targets hydrologically consequential reaches (rather than simply redistributing sites spatially), we validated selected locations against an independent reference distribution using the NWM streamflow. For each selected site and each reference PSL (n = 9,647; excluding all selected sensors to preserve spatial independence), we extracted discharge-magnitude descriptors (AMA, Q_{95}, Q_{99}, AMAX) and a flashiness index (Q_{99}/Q_{95}). Across scenarios, selected sites are systematically

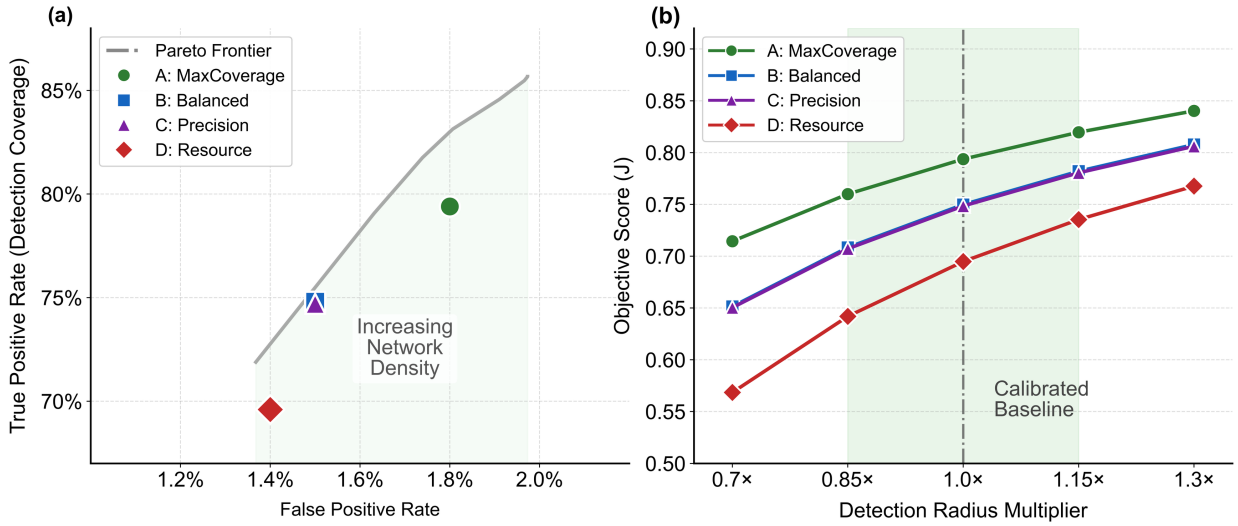

Figure 5: Network performance and sensitivity analysis. (a) True positive–false positive tradeoff showing scenario operating points along the Pareto frontier; annotation indicates direction of increasing network density. (b) Objective score sensitivity to detection radius multiplier (0.7×–1.3×); shaded region indicates ±15% robust zone around the semi-variogram-calibrated baseline (dashed line).

located on higher-flow reaches than the reference distribution, with statistically significant shifts (two-sided Mann–Whitney U; $p < 0.001$; Table 6) and moderate effect sizes by Cliff's δ, indicating that Q_{99} and AMAX are typically higher at selected sites (Table 6). This pattern strengthens under tighter budgets: smaller designs concentrate on reaches with the largest long-record flows (higher Q_{99} and AMAX), whereas larger designs extend into smaller tributaries to recover spatial coverage, yielding a clear size–selectivity tradeoff consistent with greedy selection under a risk-weighted objective (Table 6).

Table 6: NWM Retrospective Validation Results Across Operational Scenarios. N is the number of selected sites with valid NWM metrics; Q_{99} is the 99th-percentile discharge; AMAX is the mean annual maximum (mean of annual peaks). Cliff's δ compares selected vs. reference ($\delta > 0$ indicates higher flows at selected sites). Above P75/P90 is the share of selected sites with Q_{99} at or above the reference 75th/90th percentile. Effect-size bins use $|\delta|$: negligible < 0.147, small 0.147–< 0.33, medium 0.33–< 0.474, large ≥ 0.474.

Scenario	N	Q_{99} Median (m^3/s)	AMAX Median (m^3/s)	Cliff's δ	Effect Size	Above P75	Above P90
A	454	3.18	5.82	0.392	Medium	53.70%	21.60%
B	284	4.37	8.14	0.444	Medium	59.50%	23.90%
C	283	4.39	8.21	0.443	Medium	59.70%	24.00%
D	193	5.03	9.47	0.472	Medium	62.20%	26.90%
Reference	9,647	0.52	0.89	—	—	25.00%	10.00%

The cumulative distribution functions (CDFs) provide a complementary view: for discharge-magnitude metrics, scenario curves are shifted toward higher flows relative to the reference, while the flashiness ratio (Q_{99}/Q_{95}), which measures how sharply the upper tail of the flow distribution peaks, shows near overlap across scenarios. This indicates that the optimization is largely agnostic to flow regime variability and instead prioritizes large-magnitude event exposure (Figure 7).

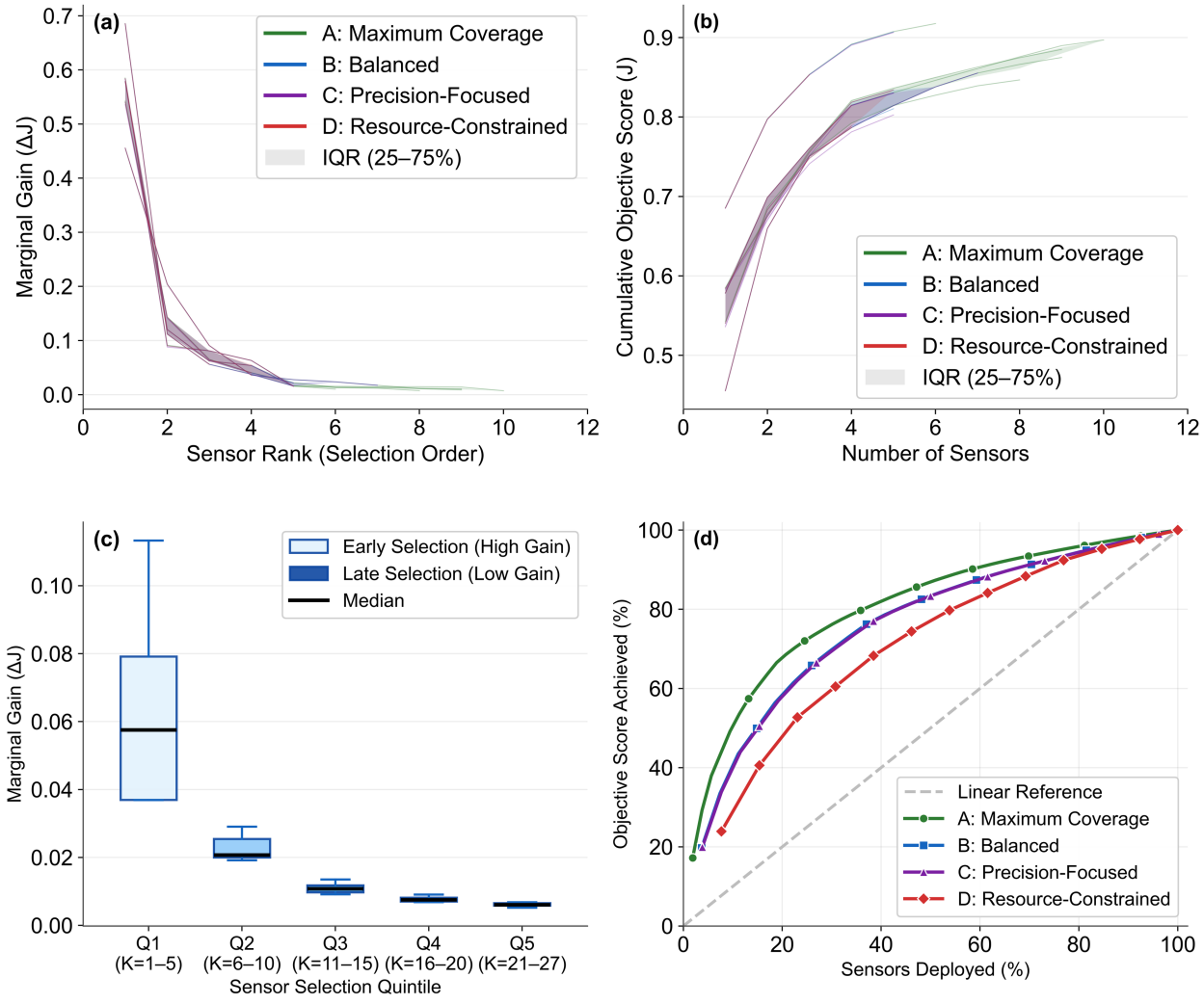

Figure 6: Submodularity verification and diminishing returns analysis. (a) Per-basin marginal gain trajectories showing decay below $\Delta J = 0.05$ by the third sensor; shaded region represents interquartile range. (b) Cumulative objective score versus network size demonstrating asymptotic convergence. (c) Marginal gain distribution by sensor selection quintile; gradient shading reflects diminishing value from early (Q1) to late (Q5) placements. (d) Normalized cumulative value curves; dashed line indicates linear reference where each sensor contributes equally.

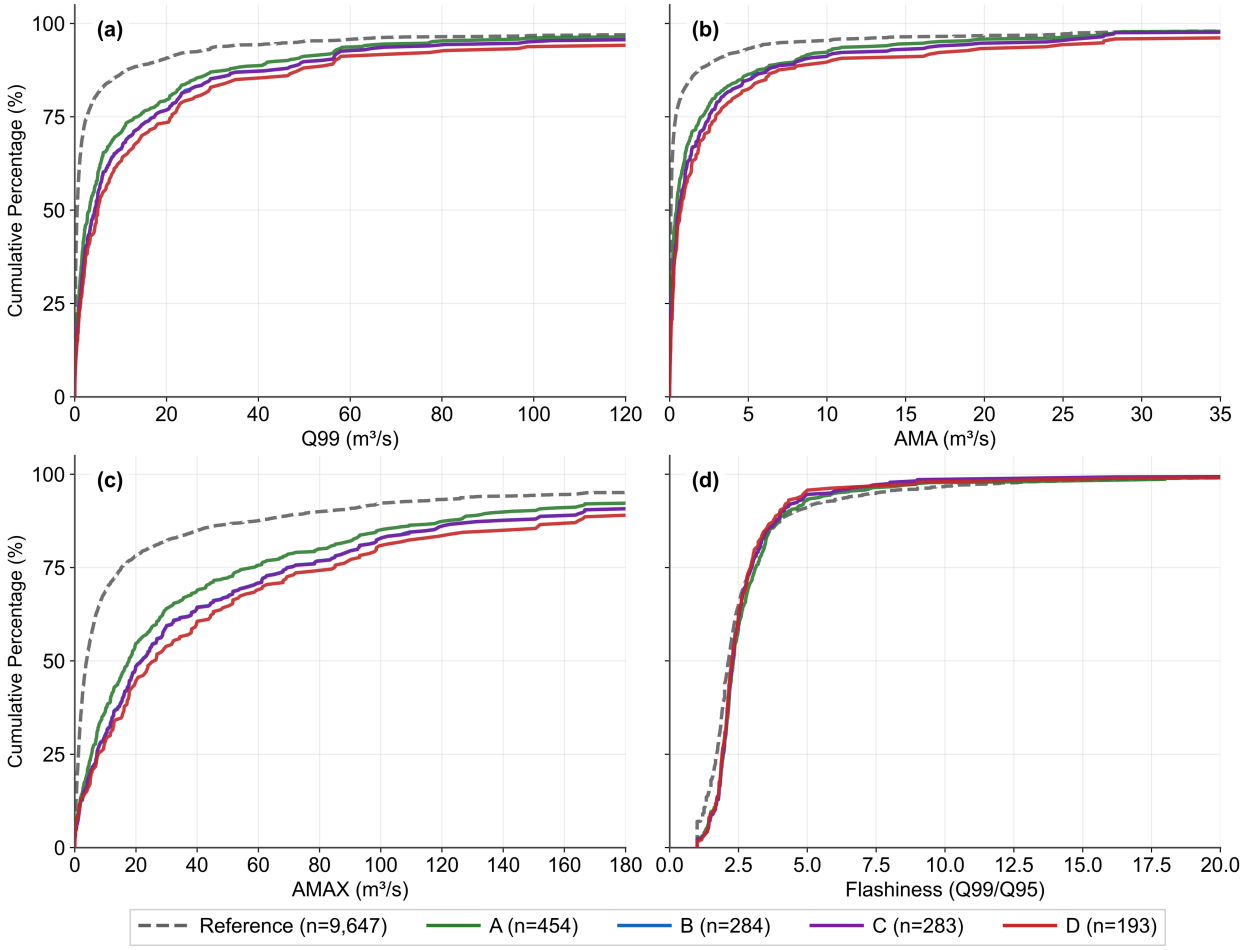

Figure 7: Cumulative distribution functions of NWM Retrospective v3.0 flow metrics (1979 to 2023) for selected sensor locations across scenarios versus an independent reference sample (n = 9,647): (a) Q_{99} (99th percentile discharge), (b) AMA (annual mean average discharge), (c) AMAX (annual peak discharge averaged across 44 water years), and (d) flashiness index (Q_{99}/Q_{95} ratio).

4.8 Integration with Existing Infrastructure

4.8.1 Baseline USGS Coverage Assessment

Within the study area, the 69 operational USGS streamgages provide partial coverage of the risk-weighted flood domain (Figure 8a–b). Using the semi-variogram-calibrated detection radius (Section 3), baseline coverage leaves substantial risk exposure unmonitored, motivating complementary deployment targeted to remaining monitoring gaps rather than uniform densification.

4.8.2 Incremental Coverage from Optimized Networks

Across scenarios, augmenting the USGS network with the optimized multi-sensor designs yields large incremental gains in risk-weighted coverage. Combined USGS-plus-proposed coverage ranged from 88.1% (Scenario D, 216 sensors) to 96.7% (Scenario A, 491 sensors), representing incremental gains of 43.8–52.4 percentage points over the USGS baseline (Figure 8b).

4.8.3 Sensor Functional Classification

Sentinels provide independent coverage in unmonitored headwater reaches across all scenarios ranging from 44 to 49% (Figure 8c). Cascade Sentinels (~26%) enable upstream early warning relative to USGS stations; Gap-Fillers (16–17%) address coverage discontinuities on tributaries between existing stations; and Validators (9–13%) co-locate with USGS sites for measurement redundancy and backup monitoring. This distribution proved robust across scenarios, varying by less than 6 percentage points between Maximum Coverage and Resource-Constrained configurations. The underlying upstream determinations were robust: across scenarios, 79–81% of the sensor–gage upstream relationships satisfied the high-confidence criterion (≥3 of the four hydrological indicators in agreement), with the remainder meeting the medium-confidence criterion (2 indicators) and none classified low-confidence.

4.8.4 Flood Warning Cascade Architecture

Cascade Sentinels explain a simple cascade-warning concept, where detections on upstream tributaries precede impacts at downstream USGS gages. Lead times were estimated from sinuosity-adjusted separation and stream-order–based wave celerity (Section 3), yielding median warning intervals of ~2 hours across scenarios (Table 7). With mean sensor-to-USGS distances of 15.5–18.4 km, these lead times are operationally relevant for typical headwater time-to-peak windows, and the slight increase under resource constraints reflects retention of higher-leverage upstream placements at greater separation distances.

Table 7: Cascade Sentinel lead time statistics by operational scenario. Cascade Sentinels are proposed sensors located within the detection radius of, and hydrologically upstream of, an existing USGS streamgage. Median lead time is the estimated flood-wave travel time from each Cascade Sentinel to its nearest downstream USGS station (Section 3), with the interquartile range (IQR) in parentheses; mean distance is the corresponding mean sensor-to-station separation.

Scenario	Cascade Sentinels	Median Lead Time, h (IQR)	Mean Distance (km)
A: Maximum Coverage	126	1.7 (0.8–3.2)	15.5
B: Balanced	82	1.8 (1.0–3.2)	16.8
C: Precision-Focused	81	1.9 (1.0–3.2)	17.0
D: Resource-Constrained	56	1.9 (1.1–3.3)	18.4

4.8.5 Implications for Deployment

Operationally, the proposed optimized networks achieve 88–97% flood risk coverage with sensor densities of one per 70–160 km^2, compared to one USGS station per 500 km^2 in the existing network. Across budget scenarios, the added deployments retain a stable functional composition: headwater sentinels, cascade sentinels for upstream warning, gap-fillers, and validators, indicating that scenario choice primarily trims marginal sites rather than changing the network's role structure.

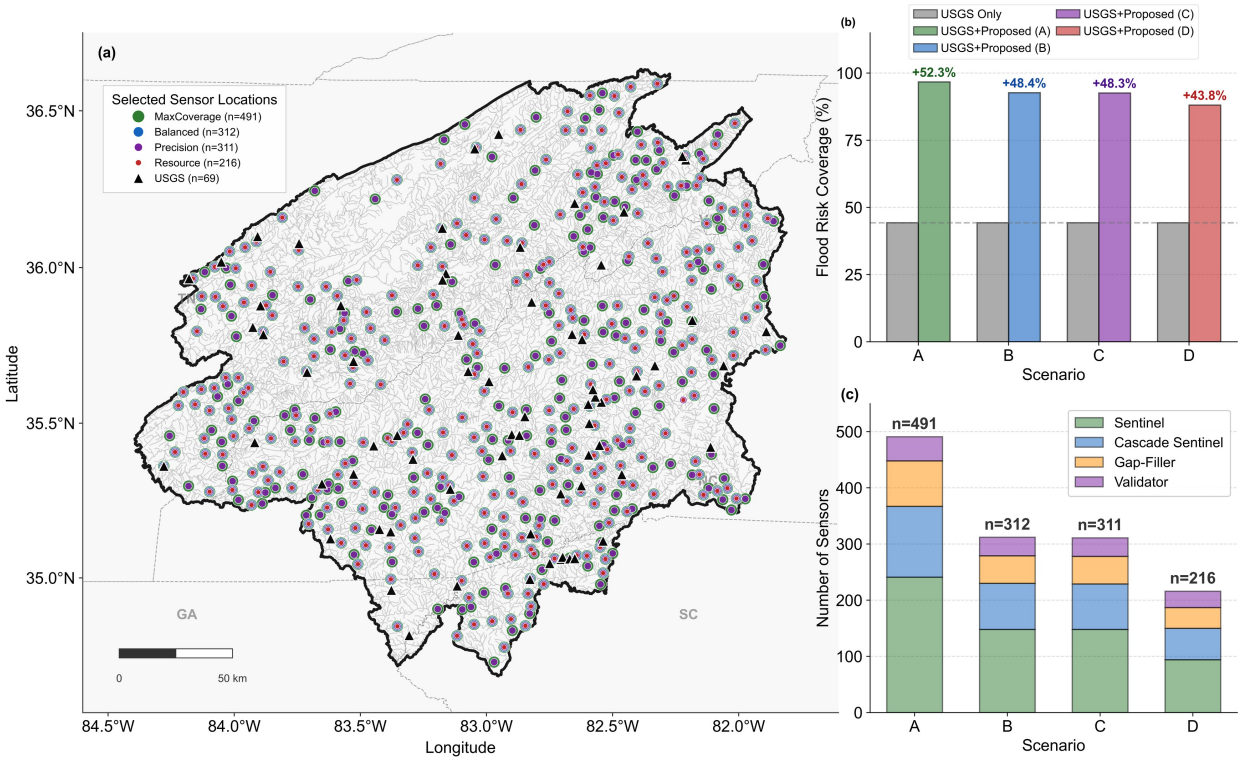

Figure 8: Integration of optimized sensor network with existing USGS stream gage infrastructure. (a) Scenario selections overlaid with USGS gages. (b) Flood risk coverage comparison showing USGS baseline (44.3%, gray) versus combined USGS+proposed networks by scenario. (c) Functional roles of selected sites from multi-indicator upstream analysis (sentinel, cascade sentinel, gap-filler, validator).

5 Discussion

5.1 Synthesis and Design Trade-offs

This study advances hydrometric network planning by combining three elements within one decision framework: coordinated multi-sensor placement, validation against long-record hydrology, and explicit complementarity with existing infrastructure. The core result is that detection performance depends more on *where* sensors are placed and coupled than on network size alone. Across scenarios, multi-sensor designs outperform both random and uniform-grid baselines (Table 4), while grid allocation is consistently lower than random, confirming that regular spacing is a poor proxy in heterogeneous flood-risk landscapes. The spatial pattern is also non-random: selected sites cluster along dominant risk corridors and remain nested across budgets (Figure 4a), and most selected locations support co-located sensing (Table 5), indicating that coordinated

placement, not simple densification, drives gains (Castillo-Effer, Quintela, Moreno, Jordan, & Westhoff, 2004; Oh & Bartos, 2025; Krabbenhoft et al., 2022). This supports recent calls for strategic augmentation of legacy networks rather than incremental expansion by count alone (Andrews & Grantham, 2024; Krabbenhoft et al., 2022).

Scenario behavior further shows a practical design trade-space rather than a single optimum. Increasing false-positive penalization beyond moderate levels produces near-identical solutions (Table 3), suggesting a robust plateau once low-value candidates are screened. This contrasts with information-theoretic siting approaches that can be sensitive to weighting choices (Mishra & Coulibaly, 2009; Alfonso et al., 2010; Keum & Coulibaly, 2017). Finally, the objective score trajectories and marginal-gain decay (Figure 6), together with empirical submodularity checks (Table 3), support greedy submodular maximization as an appropriate solution: early placements capture most network value, while later additions primarily refine residual gaps (Nemhauser et al., 1978; Krause, Leskovec, et al., 2008; Oh & Bartos, 2025).

5.2 Multi-Sensor Synergies

Our core result is that the benefit of multi-sensor design becomes more pronounced as resources tighten, because the solution preferentially retains locations where cross-sensor corroboration adds the most detection value (Table 4). The selected networks remain co-location dominant across scenarios (Table 5; Figure 4), and the marginal-value structure indicates that coordinated sensing at high-information sites contributes more than broad single-sensor distribution (Figure 6). In practical terms, our framework favors sites where complementary measurements reduce ambiguity in flood detection under operational constraints.

This behavior is physically consistent with known modality strengths and limitations. Water level sensors provide rapid local response but are vulnerable to backwater effects, debris interference, and hysteresis; discharge sensors integrate upstream behavior but rely on stable hydraulic controls and rating assumptions; and camera systems provide direct visual corroboration yet depend on illumination, visibility, and installation geometry (Perks, Russell, & Large, 2016; Tauro, Selker, et al., 2018; Herschy, 2009). Prior non-contact monitoring studies show that imaging can provide scalable event observations in difficult gauging environments (Tauro, Porfiri, & Grimaldi, 2016; Eltner, Sardemann, & Grundmann, 2020; Dolcetti, Hortobágyi, Perks, Tait, & Dervilis, 2022; Chen et al., 2024). Our results align with that evidence, but also extend it by showing that imaging yields the strongest operational value when jointly optimized with water level and discharge sensing within a shared risk- and cost-constrained objective (Table 5; Figure 4).

Co-location therefore improves reliability: cross-modal agreement reduces false alarms and expands effective detection beyond any single sensor. The co-location dominance indicates preference for hydrologically informative sites over uniform dispersal, consistent with sensor-fusion principles of consistency checks and probabilistic updating (Castillo-Effer et al., 2004; Krzhizhanovskaya et al., 2011). The suitability models (Section 3) explain why this pattern emerges. Discharge suitability favors drainage area and flow accumulation (Rantz et al., 1982; Sauer & Turnipseed, 2010), water level suitability emphasizes low slope and topographic wetness index (Beven & Kirkby, 1979), and camera suitability favors gentle terrain and access/field-of-view constraints. Because stream order variable was used for all three, intermediate-order reaches become recurrent co-location targets where feasibility and information content align, supporting targeted observation over blanket densification consistent with hydrologically significant reaches (Wohl, 2017).

5.3 Relation to Prior Hydrometric Network-Design Approaches

This framework advances hydrometric network design by integrating (i) a risk-weighted flood-detection objective, (ii) coordinated multi-sensor placement, and (iii) validation against long retrospective hydrologic records, and makes evaluation explicitly task-relevant. Information-theoretic approaches emphasize repre-

sentativeness and redundancy reduction (Mishra & Coulibaly, 2009; Alfonso et al., 2010; Samuel et al., 2013), but they can under-prioritize flood-generating headwaters when local variability is constrained, and the goal is onset detection. Our formulation instead prioritizes flood-prone reaches and tributary structure, consistent with the idea that inland flood monitoring should reflect dendritic propagation and onset dynamics (Gourley et al., 2017; Emerton et al., 2016; Nearing et al., 2024).

This framework also aligns with decision-oriented, multi-objective location of sensors for flood contexts. Tien et al. (2023) optimize real-time water-level sensors for coastal communities across coverage and uncertainty together with hazard, serviceability, and social vulnerability, emphasizing feasible Pareto choices for staged deployment; the same decision logic applies inland under access, maintenance, and governance constraints. We extend this logic to river networks by coordinating water level–discharge–camera deployment and adding explicit false-alarm penalties, tying network value to a detection task and an operational error budget.

Methodologically, this work builds on scalable optimization. Submodular placement has proven effective for large candidate sets and diminishing-returns behavior, including hydrologic augmentation guided by retrospective simulations (Krause, Leskovec, et al., 2008; Oh & Bartos, 2025), and our results show the same structure while shifting the objective from reconstruction-focused monitoring to early-warning detection under explicit false alarm constraints. Observability-based placement provides another complementary stream of research, demonstrating that physically motivated objectives can outperform heuristic siting in river-network problems (Bartos & Kerkez, 2021). Finally, the existing infrastructure-integration analysis responds to criticism that legacy (USGS) networks reflect historical decisions and institutional convenience and evaluates augmentations by complementarity rather than sensor count (Krabbenhoft et al., 2022; Andrews & Grantham, 2024).

5.4 Operational Implications for Flood Early Warning

Operationally, the results support a cascade warning architecture in which upstream sensors deliver actionable lead time for both headwater residents and downstream communities. This dual benefit is critical: during Hurricane Helene, 43 of North Carolina's 107 storm-related fatalities occurred in Buncombe County, where steep headwater tributaries afforded virtually no lead time for residents at the point of flood origin (North Carolina Department of Health and Human Services, 2025; Hagen et al., 2026). In these settings, warning value is constrained by short response times and sparse observation in small tributaries, so strategic extension into headwaters can outperform densifying already-monitored mainstems (Emerton et al., 2016; Krabbenhoft et al., 2022). The estimated lead times reinforce that useful warning windows are on the order of hours, and that low-latency detection and communication can matter as much as hydrologic skill (Hapuarachchi, Wang, & Pagano, 2011; Gourley et al., 2017). Diminishing returns provides a basis for staged deployment: prioritize a first segment of high-leverage sites, evaluate performance and maintenance burden, then expand adaptively. This aligns with evidence that early warning is highly cost-effective when designed around operational constraints and decision timelines (Hallegatte, 2012; World Meteorological Organization, 2022). Functional roles (e.g., Sentinel, Cascade Sentinel, Gap Filler, Validator) map outputs to workflows, including redundancy and corroboration that can reduce false alarms (Werner & Cranston, 2009; Krzhizhanovskaya et al., 2011).

5.5 Limitations and Future Directions

The framework is extensible, but some limitations motivate clear next steps. First, semi-variogram radii provide a data-driven scale but assumes within-basin stationarity of risk autocorrelation; physiographic gradients, storm-type differences, and human modification motivate reach-specific footprints (Matheron, 1963; Cressie, 1993). Event-adaptive footprints calibrated from floods could improve realism and reduce false alarms. Similarly, risk proxies may need updating under nonstationary extremes. The current isotropic

exponential distance–decay model is intentionally simple; operational extensions should condition detection on flowline connectivity and, where feasible, travel time rather than Euclidean distance alone, and allow anisotropy along valleys versus across divides.

Second, the fusion model assumes conditional independence with fixed sensor-quality parameters; future work should represent correlated failures (e.g., debris affecting water level and cameras) and regime-dependent camera reliability (night, fog, glare), supported by field calibration and performance-conditioned priors and updated likelihood models that encode correlated reliability (Tauro, Piscopia, & Grimaldi, 2017; Chen et al., 2024). Moving from allocation to deployment also requires optimizing temporal sampling, communications latency, maintenance burden, privacy constraints, and life-cycle cost.

Third, while the NWM Retrospective v3.0 offers long-record consistency, it is simulated streamflow (no streamflow assimilation in the retrospective archive); thus NWM-based "hydrologic significance" can reflect model bias, often strongest in small headwaters (Cosgrove et al., 2024). Because the risk surface drives the objective, reported performance is conditional on that representation and may be optimistic in-sample; stronger evidence requires out-of-sample tests (temporal and/or spatial holdout) and sensitivity to alternative risk constructions and weights (Hastie, Tibshirani, & Friedman, 2009).

Fourth, upstream role assignments currently rely on robust spatial proxies (elevation differencing and basin proximity); a practical refinement is explicit network routing (e.g., NHDPlus/Hydrologic sequence number) with path validation before cascade-role assignment and lead-time computation. Transferability beyond the Southern Appalachians is a priority: snowmelt, regulation, and monsoon regimes may require re-tuned suitability weights, different risk proxies, and travel-time formulations aligned with dominant flood physics and changing extremes (Merz & Blöschl, 2005; Tabari, 2020). Additionally, while the optimization prioritizes sites that maximize basin-wide flood detection coverage, the current validation evaluates performance through aggregate streamflow statistics at the basin outlet scale and does not explicitly test the framework's utility for localized flash flood warnings in headwater areas where concentration times may be under one hour. Coupling the placement framework with a real-time flood routing model would enable direct assessment of site-specific warning windows for flash-flood-prone headwater communities.

Finally, weaker differentiation in flashiness points to a clear extension for short-duration surge settings: incorporate hydrograph dynamics, such as rise time or flashiness indicators directly into the objective or as explicit constraints (Baker et al., 2004; Sturdevant-Rees et al., 2001). Reproducibility also warrants explicit treatment: QR with column pivoting can be sensitive to numerical precision, and stratified sampling introduces controlled randomness. To enable independent verification, document and share the exact random-number settings used for sampling, the selected candidate subsets, intermediate artifacts (e.g., pivot orderings), and the fully specified computing environment (e.g., containers) so analyses can be rerun consistently across platforms (Golub & Van Loan, 2013; Stevens & Olsen, 2004; Sandve, Nekrutenko, Taylor, & Hovig, 2013).

6 Conclusion

This study advances inland flood monitoring by treating network expansion on dendritic river systems as a *hydrologically informed detection problem*, where performance is governed by which river segments are observed rather than how many sensors are deployed. We develop a basin-by-basin, risk-weighted multi-sensor placement framework and show that greedy submodular optimization yields scenario-tunable networks that are computationally tractable and operationally interpretable. Across alternative management priorities, the solutions repeatedly recover a stable backbone of high-leverage sites and exhibit strong diminishing returns, which supports phased deployment in practice because early investments capture most detection value and later additions primarily close residual gaps. In the same setting, spatially regular allocations underperform because they do not respect the strong heterogeneity of flood risk across the river network.

We further evaluate whether the selected sites are hydrologically meaningful and whether they complement existing infrastructure. Long-record validation using the NWM Retrospective v3.0 indicates that selected locations align with higher-flow river segments relative to an independent reference distribution, supporting that the designs target flood-relevant reaches rather than reflecting spatial artifacts. Integration with the existing USGS gage network shows that the optimized deployments function as modular expansions that reduce monitoring deserts and support an upstream-to-downstream cascade warning concept, expanding risk-weighted coverage from the USGS-only baseline to near-complete coverage in the combined system and yielding median upstream lead times on the order of about 2 hours. Overall, the framework provides a general-purpose blueprint for directing new flood sensing investments toward measurable early-warning gains, with transparent tradeoffs that can be adapted across regions and operational constraints.

Data Availability

Data and codes would be made available upon publication. The underlying source data are derived from the following publicly available sources: the NHDPlus High Resolution hydrographic network (Moore et al., 2025); the USGS 3D Elevation Program 10-m digital elevation model (U.S. Geological Survey, 2019); the FEMA National Risk Index (Federal Emergency Management Agency, 2025); USGS streamgage locations from the National Water Information System (`https://waterdata.usgs.gov/nwis`); Multi-Radar Multi-Sensor Quantitative Precipitation Estimates from NOAA National Severe Storms Laboratory (`https://mrms.nssl.noaa.gov`); and the NOAA National Water Model Retrospective Analysis v3.0 accessed via Amazon Web Services Open Data (`https://registry.opendata.aws/nwm-archive/`) (Cosgrove et al., 2024).

Acknowledgments

This research was supported by the College Academy of Research, Scholarship, and Creative Activity (CARSCA)—#480 Proposal A11000-204109-100, The University of Alabama. The authors declare no competing interests.

References

Addor, N., Newman, A. J., Mizukami, N., & Clark, M. P. (2017). The CAMELS data set: Catchment attributes and meteorology for large-sample studies. *Hydrology and Earth System Sciences*, *21*(10), 5293–5313. https://doi.org/10.5194/hess-21-5293-2017

Alfonso, L., Lobbrecht, A., & Price, R. (2010). Information theory-based approach for location of monitoring water level gauges in polders. *Water Resources Research*, *46*(3), W03528. https://doi.org/10.1029/2009WR008101

Amanambu, A. C., Obarein, O. A., Mossa, J., Li, L., Ayeni, S. S., Balogun, O., . . . Ochege, F. U. (2020). Groundwater system and climate change: Present status and future considerations. *Journal of Hydrology*, *589*, 125163. https://doi.org/10.1016/j.jhydrol.2020.125163

Andrews, L., & Grantham, T. E. (2024). Strategic stream gauging network design for sustainable water management. *Nature Sustainability*, *7*, 714–723. https://doi.org/10.1038/s41893-024-01357-z

Ashley, S. T., & Ashley, W. S. (2008). Flood fatalities in the United States. *Journal of Applied Meteorology and Climatology*, *47*(3), 805–818. https://doi.org/10.1175/2007JAMC1611.1

Baker, D. B., Richards, R. P., Loftus, T. T., & Kramer, J. W. (2004). A new flashiness index: Characteristics and applications to midwestern rivers and streams. *Journal of the American Water Resources Association*, *40*(2), 503–522. https://doi.org/10.1111/j.1752-1688.2004.tb01046.x

Bartos, M., & Kerkez, B. (2021). Observability-based sensor placement improves contaminant tracing in river networks. *Water Resources Research*, *57*(7), e2020WR029551. https://doi.org/10.1029/2020WR029551

Beven, K. J., & Kirkby, M. J. (1979). A physically based, variable contributing area model of basin hydrology. *Hydrological Sciences Bulletin*, *24*(1), 43–69. https://doi.org/10.1080/02626667909491834

Britannica. (2024). *Hurricane Helene*. Encyclopedia Britannica. Retrieved from https://www.britannica.com/event/Hurricane-Helene

Businger, P., & Golub, G. H. (1965). Linear least squares solutions by Householder transformations. *Numerische Mathematik*, *7*, 269–276. https://doi.org/10.1007/BF01436084

Castillo-Effer, M., Quintela, D. H., Moreno, W., Jordan, R., & Westhoff, W. (2004). Wireless sensor networks for flash-flood alerting. In *Proceedings of the fifth IEEE International Caracas Conference on Devices, Circuits and Systems* (Vol. 1, pp. 142–146). https://doi.org/10.1109/ICCDCS.2004.1393370

Chen, M., Chen, H., Wu, Z., Huang, Y., Zhou, N., & Xu, C.-Y. (2024). A review on the video-based river discharge measurement technique. *Sensors*, *24*(14), 4655. https://doi.org/10.3390/s24144655

Chow, V. T., Maidment, D. R., & Mays, L. W. (1988). *Applied hydrology*. McGraw-Hill.

Cliff, N. (1993). Dominance statistics: Ordinal analyses to answer ordinal questions. *Psychological Bulletin*, *114*(3), 494–509. https://doi.org/10.1037/0033-2909.114.3.494

Cochran, W. G. (1977). *Sampling techniques* (3rd ed.). Wiley.

Cosgrove, B., Gochis, D., Flowers, T., Dugger, A., Ogden, F., Graziano, T., ... others (2024). NOAA's National Water Model: Advancing operational hydrology through continental-scale modeling. *Journal of the American Water Resources Association*, *60*(3), 247–272. https://doi.org/10.1111/1752-1688.13184

Cressie, N. A. C. (1993). *Statistics for spatial data* (Rev. ed.). Wiley. https://doi.org/10.1002/9781119115151

Dolcetti, G., Hortobágyi, B., Perks, M., Tait, S. J., & Dervilis, N. (2022). Using noncontact measurement of water surface dynamics to estimate river discharge. *Water Resources Research*, *58*, e2022WR032829. https://doi.org/10.1029/2022WR032829

Dunne, T., & Leopold, L. B. (1978). *Water in environmental planning*. W. H. Freeman.

Eltner, A., Sardemann, H., & Grundmann, J. (2020). Technical note: Flow velocity and discharge measurement in rivers using terrestrial and unmanned-aerial-vehicle imagery. *Hydrology and Earth System Sciences*, *24*, 1429–1445. https://doi.org/10.5194/hess-24-1429-2020

Emerton, R. E., Stephens, E. M., Pappenberger, F., Pagano, T. C., Weerts, A. H., Wood, A. W., ... Cloke, H. L. (2016). Continental and global scale flood forecasting systems. *Wiley Interdisciplinary Reviews: Water*, *3*(3), 391–418. https://doi.org/10.1002/wat2.1137

Farahmand, H., Liu, X., Dong, S., Mostafavi, A., & Gao, J. (2022). A network observability framework for sensor placement in flood control networks to improve flood situational awareness and risk management. *Reliability Engineering & System Safety*, *221*, 108366. https://doi.org/10.1016/j.ress.2022.108366

Federal Emergency Management Agency. (2025, December). *National Risk Index: Technical documentation* (Tech. Rep.). U.S. Department of Homeland Security. Retrieved from https://www.fema.gov/sites/default/files/documents/fema_national-risk-index_technical-documentation.pdf (Version 1.20)

Fekete, B. M., Robarts, R. D., Kumagai, M., Nachtnebel, H.-P., Odada, E., & Zhulidov, A. V. (2015). Time for in situ renaissance. *Science*, *349*(6249), 685–686. https://doi.org/10.1126/science.aac7358

Gaffin, D. M., & Hotz, D. G. (2000). A precipitation and flood climatology with synoptic features of heavy rainfall across the southern Appalachian Mountains. *National Weather Digest*, *24*(3), 3–15. Retrieved from https://www.weather.gov/mrx/heavyrainclimo

Golden, H. E., Christensen, J. R., McMillan, H. K., et al. (2025). Advancing the science of headwater streamflow for global water protection. *Nature Water*, *3*, 16–26. https://doi.org/10.1038/s44221-024-00351-1

Golub, G. H., & Van Loan, C. F. (2013). *Matrix computations* (4th ed.). Johns Hopkins University Press. https://doi.org/10.56021/9781421407944

Gourley, J. J., Flamig, Z. L., Vergara, H., Kirstetter, P.-E., Clark, R. A., Argyle, E., ... Howard, K. W. (2017). The FLASH project: Improving the tools for flash flood monitoring and prediction across the United States. *Bulletin of the American Meteorological Society*, *98*(2), 361–372. https://doi.org/10.1175/BAMS-D-15-00247.1

Hagen, A. B., Cangialosi, J. P., Chenard, M., Alaka, L., & Delgado, S. (2026). *Hurricane Helene (AL092024, 24–27 September 2024)* (Tropical Cyclone Report). National Oceanic and Atmospheric Administration, National Hurricane Center. Retrieved from https://www.nhc.noaa.gov/data/tcr/AL092024_Helene.pdf

Hallegatte, S. (2012). *A cost effective solution to reduce disaster losses in developing countries: Hydrometeorological services, early warning, and evacuation* (World Bank Policy Research Working Paper 6058). The World Bank. Retrieved from https://doi.org/10.1596/1813-9450-6058 https://doi.org/10.1596/1813-9450-6058

Hapuarachchi, H. A. P., Wang, Q. J., & Pagano, T. C. (2011). A review of advances in flash flood forecasting. *Hydrological Processes*, *25*(18), 2771–2784. https://doi.org/10.1002/hyp.8040

Hastie, T., Tibshirani, R., & Friedman, J. (2009). *The elements of statistical learning: Data mining, inference, and prediction* (2nd ed.). Springer. https://doi.org/10.1007/978-0-387-84858-7

Herschy, R. W. (2009). *Streamflow measurement* (3rd ed.). CRC Press. https://doi.org/10.1201/9781482265880

Kabi, J. N., wa Maina, C., Mharakurwa, E. T., & Mathenge, S. W. (2023). Low cost, LoRa based river water level data acquisition system. *HardwareX*, *14*, e00414. https://doi.org/10.1016/j.ohx.2023.e00414

Keum, J., & Coulibaly, P. (2017). Information theory-based decision support system for integrated design of multivariable hydrometric networks. *Water Resources Research*, *53*(7), 6239–6259. https://doi.org/10.1002/2016WR019981

Krabbenhoft, C. A., Allen, G. H., Lin, P., Godsey, S. E., Allen, D. C., Burrows, R. M., ... Olden, J. D. (2022). Assessing placement bias of the global river gauge network. *Nature Sustainability*, *5*(7), 586–592. https://doi.org/10.1038/s41893-022-00873-0

Krause, A., & Golovin, D. (2014). Submodular function maximization. In *Tractability: Practical approaches to hard problems* (pp. 71–104). Cambridge University Press. https://doi.org/10.1017/CBO9781139177801.004

Krause, A., Leskovec, J., Guestrin, C., VanBriesen, J., & Faloutsos, C. (2008). Efficient sensor placement optimization for securing large water distribution networks. *Journal of Water Resources Planning and Management*, *134*(6), 516–526. https://doi.org/10.1061/(ASCE)0733-9496(2008)134:6(516)

Krause, A., Singh, A., & Guestrin, C. (2008). Near-optimal sensor placements in Gaussian processes: Theory, efficient algorithms and empirical studies. *Journal of Machine Learning Research*, *9*, 235–284. Retrieved from https://www.jmlr.org/papers/v9/krause08a.html

Krzhizhanovskaya, V. V., Shirshov, G. S., Melnikova, N. B., Belleman, R. G., Rusadi, F. I., Broekhuijsen, B. J., et al. (2011). Flood early warning system: Design, implementation and computational modules. *Procedia Computer Science*, *4*, 106–115. https://doi.org/10.1016/j.procs.2011.04.012

Le Coz, J., Hauet, A., Pierrefeu, G., Dramais, G., & Camenen, B. (2010). Performance of image-based velocimetry (LSPIV) applied to flash-flood discharge measurements in Mediterranean rivers. *Journal*

of Hydrology, *394*, 42–52. https://doi.org/10.1016/j.jhydrol.2010.05.049

Lighthill, M. J., & Whitham, G. B. (1955). On kinematic waves. I. Flood movement in long rivers. *Proceedings of the Royal Society of London. Series A*, *229*(1178), 281–316. https://doi.org/10.1098/rspa.1955.0088

Mann, H. B., & Whitney, D. R. (1947). On a test of whether one of two random variables is stochastically larger than the other. *Annals of Mathematical Statistics*, *18*(1), 50–60. https://doi.org/10.1214/aoms/1177730491

Maranzoni, A., D'Oria, M., & Rizzo, C. (2023). Quantitative flood hazard assessment methods: A review. *Journal of Flood Risk Management*, *16*(1), e12855. https://doi.org/10.1111/jfr3.12855

Massey, F. J. (1951). The Kolmogorov-Smirnov test for goodness of fit. *Journal of the American Statistical Association*, *46*(253), 68–78. https://doi.org/10.1080/01621459.1951.10500769

Matheron, G. (1963). Principles of geostatistics. *Economic Geology*, *58*(8), 1246–1266. https://doi.org/10.2113/gsecongeo.58.8.1246

McCabe, M. F., Rodell, M., Alsdorf, D. E., Miralles, D. G., Uijlenhoet, R., Wagner, W., ... Wood, E. F. (2017). The future of Earth observation in hydrology. *Hydrology and Earth System Sciences*, *21*(7), 3879–3914. https://doi.org/10.5194/hess-21-3879-2017

Merz, R., & Blöschl, G. (2005). Flood frequency regionalization—spatial proximity vs. catchment attributes. *Journal of Hydrology*, *302*(1–4), 283–306. https://doi.org/10.1016/j.jhydrol.2004.07.018

Milly, P. C. D., Wetherald, R. T., Dunne, K. A., & Delworth, T. L. (2002). Increasing risk of great floods in a changing climate. *Nature*, *415*(6871), 514–517. https://doi.org/10.1038/415514a

Mishra, A. K., & Coulibaly, P. (2009). Developments in hydrometric network design: A review. *Reviews of Geophysics*, *47*(2), RG2001. https://doi.org/10.1029/2007RG000243

Moore, R. B., McKay, L. D., Rea, A. H., Bondelid, T. R., Price, C. V., Dewald, T. G., & Hayes, L. (2025). *User's guide for the National Hydrography Dataset Plus High Resolution (NHDPlus HR)* (Scientific Investigations Report Nos. 2025–5031). U.S. Geological Survey. Retrieved from https://doi.org/10.3133/sir20255031 https://doi.org/10.3133/sir20255031

Muste, M., Fujita, I., & Hauet, A. (2008). Large-scale particle image velocimetry for measurements in riverine environments. *Water Resources Research*, *44*, W00D19. https://doi.org/10.1029/2008WR006950

Nearing, G., Cohen, D., Dube, V., Gauch, M., Gilon, O., Harrigan, S., ... Matias, Y. (2024). Global prediction of extreme floods in ungauged watersheds. *Nature*, *627*(8004), 559–563. https://doi.org/10.1038/s41586-024-07145-1

Nemhauser, G. L., Wolsey, L. A., & Fisher, M. L. (1978). An analysis of approximations for maximizing submodular set functions—I. *Mathematical Programming*, *14*(1), 265–294. https://doi.org/10.1007/BF01588971

North Carolina Department of Health and Human Services. (2025). *Hurricane Helene storm related fatalities.* Retrieved from https://www.ncdhhs.gov/assistance/hurricane-helene-recovery-resources/hurricane-helene-storm-related-fatalities

O'Callaghan, J. F., & Mark, D. M. (1984). The extraction of drainage networks from digital elevation data. *Computer Vision, Graphics, and Image Processing*, *28*(3), 323–344. https://doi.org/10.1016/S0734-189X(84)80011-0

Oh, J., & Bartos, M. (2025). Scalable, adaptive and risk-informed design of hydrological sensor networks. *Nature Water*, *3*, 1144–1154. https://doi.org/10.1038/s44221-025-00496-7

Papathoma-Köhle, M., Cristofari, G., Wenk, M., & Fuchs, S. (2019). The importance of indicator weights for vulnerability indices and implications for decision making in disaster management. *International Journal of Disaster Risk Reduction*, *36*, 101103. https://doi.org/10.1016/j.ijdrr.2019.101103

Pappenberger, F., Cloke, H. L., Parker, D. J., Wetterhall, F., Richardson, D. S., & Thielen, J. (2015). The monetary benefit of early flood warnings in Europe. *Environmental Science & Policy*, *51*, 278–291. https://doi.org/10.1016/j.envsci.2015.04.016

Perks, M. T., Russell, A. J., & Large, A. R. G. (2016). Technical note: Advances in flash flood monitoring using unmanned aerial vehicles (UAVs). *Hydrology and Earth System Sciences*, *20*(10), 4005–4015. https://doi.org/10.5194/hess-20-4005-2016

Rantz, S. E., et al. (1982). *Measurement and computation of streamflow: Volume 1. Measurement of stage and discharge* (Water-Supply Paper 2175). U.S. Geological Survey. https://doi.org/10.3133/wsp2175

Romano, J., Kromrey, J. D., Coraggio, J., & Skowronek, J. (2006). Appropriate statistics for ordinal level data: Should we really be using t-test and Cohen's d for evaluating group differences on the NSSE and other surveys? In *Annual meeting of the Florida Association of Institutional Research* (pp. 1–33). Retrieved from https://www.researchgate.net/publication/237544991

Samuel, J., Coulibaly, P., & Kollat, J. B. (2013). CRDEMO: Combined regionalization and dual entropy-multiobjective optimization for hydrometric network design. *Water Resources Research*, *49*, 8070–8089. https://doi.org/10.1002/2013WR014058

Sandve, G. K., Nekrutenko, A., Taylor, J., & Hovig, E. (2013). Ten simple rules for reproducible computational research. *PLOS Computational Biology*, *9*(10), e1003285. https://doi.org/10.1371/journal.pcbi.1003285

Sauer, V. B., & Turnipseed, D. P. (2010). *Stage measurement at gaging stations* (Techniques and Methods Book 3, Chapter A7). U.S. Geological Survey. https://doi.org/10.3133/tm3A7

Seaber, P. R., Kapinos, F. P., & Knapp, G. L. (1987). *Hydrologic unit maps* (Water Supply Paper 2294). U.S. Geological Survey. https://doi.org/10.3133/wsp2294

Smakhtin, V. U. (2001). Low flow hydrology: A review. *Journal of Hydrology*, *240*(3–4), 147–186. https://doi.org/10.1016/S0022-1694(00)00340-1

Smith, J. A., Baeck, M. L., Ntelekos, A. A., Villarini, G., & Steiner, M. (2011). Extreme rainfall and flooding from orographic thunderstorms in the central Appalachians. *Water Resources Research*, *47*(4), W04514. https://doi.org/10.1029/2010WR010190

Stedinger, J. R., Vogel, R. M., & Foufoula-Georgiou, E. (1993). Frequency analysis of extreme events. In D. R. Maidment (Ed.), *Handbook of hydrology* (pp. 18.1–18.66). McGraw-Hill.

Stevens, D. L., Jr., & Olsen, A. R. (2004). Spatially balanced sampling of natural resources. *Journal of the American Statistical Association*, *99*(465), 262–278. https://doi.org/10.1198/016214504000000250

Strahler, A. N. (1957). Quantitative analysis of watershed geomorphology. *Transactions of the American Geophysical Union*, *38*(6), 913–920. https://doi.org/10.1029/TR038i006p00913

Sturdevant-Rees, P., Smith, J. A., Morrison, J., & Baeck, M. L. (2001). Tropical storms and the flood hydrology of the central Appalachians. *Water Resources Research*, *37*(8), 2143–2168. https://doi.org/10.1029/2000WR900310

Tabari, H. (2020). Climate change impact on flood and extreme precipitation increases with water availability. *Scientific Reports*, *10*(1), 13768. https://doi.org/10.1038/s41598-020-70816-2

Tarboton, D. G., Bras, R. L., & Rodriguez-Iturbe, I. (1991). On the extraction of channel networks from digital elevation data. *Hydrological Processes*, *5*(1), 81–100. https://doi.org/10.1002/hyp.3360050107

Tauro, F., Petroselli, A., & Grimaldi, S. (2018). Optical sensing for stream flow observations: A review. *Journal of Agricultural Engineering*, *49*(4), 199-206. https://doi.org/10.4081/jae.2018.836

Tauro, F., Piscopia, R., & Grimaldi, S. (2017). Streamflow observations from cameras: Large-scale particle image velocimetry or particle tracking velocimetry? *Water Resources Research*, *53*(12), 10374–10394. https://doi.org/10.1002/2017WR020848

Tauro, F., Porfiri, M., & Grimaldi, S. (2016). Surface flow measurements from drones. *Journal of Hydrology*, *540*, 240–245. https://doi.org/10.1016/j.jhydrol.2016.06.012

Tauro, F., Selker, J., van de Giesen, N., Abrate, T., Uijlenhoet, R., Porfiri, M., ... others (2018). Measurements and observations in the XXI century (MOXXI): Innovation and multi-disciplinarity to sense the hydrological cycle. *Hydrological Sciences Journal*, *63*(2), 169–196. https://doi.org/10.1080/02626667.2017.1420191

Tellman, B., Sullivan, J. A., Kuhn, C., Kettner, A. J., Doyle, C. S., Brakenridge, G. R., ... Slayback, D. A. (2021). Satellite imaging reveals increased proportion of population exposed to floods. *Nature*, *596*(7870), 80–86. https://doi.org/10.1038/s41586-021-03695-w

Tien, I., Lozano, J. M., & Chavan, A. (2023). Locating real-time water level sensors in coastal communities to assess flood risk by optimizing across multiple objectives. *Communications Earth & Environment*, *4*, 96. https://doi.org/10.1038/s43247-023-00761-1

U.S. Geological Survey. (2019). *3D Elevation Program 10-meter resolution digital elevation model.* Retrieved from https://www.usgs.gov/the-national-map-data-delivery

Werner, M., & Cranston, M. (2009). Understanding the value of radar rainfall nowcasts in flood forecasting and warning in flashy catchments. *Meteorological Applications*, *16*(1), 41–55. https://doi.org/10.1002/met.125

Wing, O. E. J., Bates, P. D., Smith, A. M., Sampson, C. C., Johnson, K. A., Fargione, J., & Morefield, P. (2018). Estimates of present and future flood risk in the conterminous United States. *Environmental Research Letters*, *13*(3), 034023. https://doi.org/10.1088/1748-9326/aaac65

Wohl, E. (2017). The significance of small streams. *Frontiers of Earth Science*, *11*, 447–456. https://doi.org/10.1007/s11707-017-0647-y

World Meteorological Organization. (2008). *Guide to hydrological practices: Volume I Hydrology from measurement to hydrological information* (6th ed.) (No. WMO-No. 168). World Meteorological Organization. Retrieved from https://library.wmo.int/records/item/35804-guide-to-hydrological-practices-volume-i

World Meteorological Organization. (2022). *Early warnings for all: The UN global early warning initiative for the implementation of climate adaptation.* WMO. Retrieved from https://wmo.int/activities/early-warnings-all

Zou, Y., & Chakrabarty, K. (2004). Sensor deployment and target localization in distributed sensor networks. *ACM Transactions on Embedded Computing Systems*, *3*(1), 61–91. https://doi.org/10.1145/972627.972631

A Supporting Information

Hydrologic and Geomorphic Variables for Sensor Suitability

The sensor suitability models (Section 3) integrate 10 hydrogeomorphic variables plus risk descriptors selected based on established literature linking each attribute to flood monitoring requirements. Table A1 presents the complete variable inventory with physical justification, mathematical transformation, and supporting literature. Variables are transformed prior to combination to account for distributional characteristics: log transformation addresses right-skewed distributions typical of drainage area and flow accumulation, while inversion ($1 - \tilde{x}$) reorients variables where low values indicate favorable conditions.

Variable Weights by Sensor Type

The suitability models apply sensor-specific weighting schemes reflecting the distinct operational requirements of each monitoring technology. Table A2 presents the weight allocation with physical justification for each sensor–variable combination. Discharge sensors are best suited at stable channel cross sections with well-defined stage–discharge relationships, which typically occur on reaches with substantial contributing area and consistent channel geometry (Rantz et al., 1982). Water level sensors, in contrast, benefit from locations where fluctuations are both amplified and practically observable, often associated with high topographic wetness and relatively low terrain slope (Beven & Kirkby, 1979). Visual flood-detection cameras require unobstructed sightlines and clear, distinguishable flood signatures, and their reliability can be reduced

Table A1: Hydrologic and geomorphic variables integrated into the multi-sensor suitability models (Section 3 of the main text). Each variable is described with its physical rationale for inclusion in flood monitoring site selection, the mathematical transformation applied prior to weighted combination (Log = log-transformed to address right-skewed distributions; Invert = inverted as $1 - \tilde{x}$ so that lower raw values yield higher suitability scores; Linear = min–max normalized without additional transformation), and the supporting literature basis.

Variable	**Description**	**Physical Rationale**	**Trans.**	**Literature**
Flow Accumulation (flowacc)	Cumulative upstream cells draining to location	Identifies flow concentration points where runoff converges; higher accumulation indicates greater flood conveyance potential	Log	O'Callaghan & Mark (1984)
Total Drainage Area (nhd_totdasqkm)	Contributing watershed area (km^2)	Controls discharge magnitude through the power-law Q–A relationship ($Q \propto A^n$); larger basins generate higher peak flows	Log	Dunne & Leopold (1978)
Strahler Stream Order (nhd_streamorder)	Hierarchical stream classification	Indicates channel size and position in network hierarchy; higher orders correspond to larger, more permanent channels suitable for monitoring	Linear	Strahler (1957)
Stream Level Distance (nhd_streamlevel)	Distance from network outlet (NHDPlus hierarchy)	Lower values indicate main-stem channels with higher flows and established infrastructure access; inverted to favor mainstems	Invert	NHDPlus hierarchy
Channel Slope (nhdplusflowline_slope)	Longitudinal stream gradient	Affects stage–discharge relationship stability; moderate slopes provide reliable rating curves for discharge estimation	Linear	WMO (2008)
Mean Annual Precip. (rain_mean)	Mean annual precipitation (mm) derived from MRMS QPE (2020–2024)	Primary driver of runoff generation; higher precipitation increases flood frequency and magnitude	Linear	Chow et al. (1988)
Topographic Wetness Index (twi)	$\ln(A/\tan\beta)$; A = catchment area, β = slope	Predicts soil saturation and surface water accumulation; high TWI indicates flood-susceptible convergent terrain	Linear	Beven & Kirkby (1979)
Terrain Slope (slope_deg)	Local surface gradient (degrees)	Low slopes promote water ponding and flood inundation; inverted to favor flat, flood-prone areas	Invert	Chow et al. (1988)
Elevation (elevation_m)	Height above sea level (m)	Valley floors and low-lying areas experience greater flood exposure; inverted to favor low elevations	Invert	FEMA (2025)
Lake Fraction (LakeFract)	Proportion of upstream area as lake/reservoir	Degrades camera-based velocimetry due to specular reflection and attenuated surface velocity signals	Linear (penalty)	Tauro et al. (2016); Le Coz et al. (2010); Muste et al. (2008)

in lacustrine or backwater-influenced settings where standing water obscures event-specific signals (Perks et al., 2016).

Table A2: Sensor-specific variable weights used in the suitability scoring models for discharge sensors, water level sensors, and visual flood-detection cameras. Weights are reported on a 0–100 scale (i.e., 100× the unitless fractional weights) and reflect the distinct operational requirements of each monitoring technology. Dashes (—) indicate variables not included in a given sensor model. The lake fraction penalty (−30*) is applied multiplicatively to camera suitability scores rather than additively. Weights for each sensor type sum to 100 before penalty application. Justifications and representative literature sources are provided for each sensor–variable combination.

Variable	**Sensor Weight**			**Justification**	**Representative**
	Disch.	**W. Level**	**Camera**		**Literature**
Flow accumulation (log)	25	15	—	Discharge sensors require substantial contributing drainage area	O'Callaghan & Mark (1984)
Drainage area (log)	20	—	15	Controls peak flow magnitude through Q–A scaling	Dunne & Leopold (1978)
Stream order	15	15	15	Higher-order streams provide stable monitoring conditions	Strahler (1957)
Stream level (inv.)	15	—	—	Mainstem channels preferred for discharge measurement	Moore et al. (2025)
Channel slope	10	—	—	Moderate slopes ensure stable rating curves	WMO (2008); Rantz et al. (1982)
Precipitation	15	15	—	Runoff driver; high precipitation = greater flood frequency	Chow et al. (1988)
TWI	—	20	20	Water level sensors benefit from topographic convergence	Beven & Kirkby (1979)
Terrain slope (inv.)	—	20	25	Flat terrain promotes ponding and camera accessibility	Chow et al. (1988)
Elevation (inv.)	—	15	25	Low elevations correspond to valley floors	FEMA (2025)
Lake fraction (penalty)	—	—	−30*	Lake surfaces degrade image velocimetry performance	Muste et al. (2008); Le Coz et al. (2010); Tauro et al. (2017)

*Applied as multiplicative penalty: $(1 - 0.30 \times \tilde{L})$ where $\tilde{L}$ is normalized lake fraction. Weights for each sensor sum to 100 before penalty application.